# A 250m annual alpine grassland AGB dataset over the Qinghai-Tibetan Plateau (2000-2019) in China based on in-situ measurements, UAV photos, and MODIS Data

Huifang Zhang [1,2,3], Zhonggang Tang[2], Binyao Wang[2], Hongcheng Kan[2] ,Yi Sun[1,2], Yu Qin[3], Baoping Meng[1,2], Meng Li[1,2], Jianjun Chen[4], Yanyan Lv[1,2], Jianguo Zhang[1,2] Shuli Niu[5], Shuhua Yi [1,2],*

[1]Institute of Fragile Eco-environment, Nantong University, 999 Tongjing Road, Nantong, Jiangsu, 226007, China
[2]School of Geographic Science, Nantong University, 999 Tongjing Road, Nantong, Jiangsu, 226007, China
[3]State Key Laboratory of Cryospheric Sciences, Northwest Institute of Eco-Environment and Resources, Chinese Academy of Sciences, 320 Donggang West Road, Lanzhou 730000, China
[4]College of Geomatics and Geoinformation, Guilin University of Technology, 12 Jiangan Road, Guilin 541004, China;
[5]Key Laboratory of Ecosystem Network Observation and Modeling, Institute of Geographic Sciences and Natural Resources Research, Chinese Academy of Sciences, Beijing, China

*Correspondence to:* Shuhua Yi (yis@ntu.edu.cn)

**Abstract.** The alpine grassland ecosystem accounts for 53% of the Qinghai-Tibet Plateau (QTP) area and is an important ecological protection barrier, but it is fragile and vulnerable to climate change. Therefore, continuous monitoring of grassland aboveground biomass (AGB) is necessary. Although many studies have mapped the spatial distribution of AGB for the QTP, the results vary widely due to the limited ground samples and mismatches with satellite pixel scales. This paper proposed a new algorithm using unmanned aerial vehicles (UAVs) as a bridge to estimate the grassland AGB on the QTP from 2000 to 2019. The innovations were as follows: 1) In terms of ground data acquisition, spatial scale matching among the traditional ground samples, UAV photos, and MODIS pixels was considered. A total of 906 pairs between field harvested AGB and UAV sub-photos, and 2,602 sets of MODIS pixel scale UAV data (over 37,000 UAV photos) were collected during 2015-2019. Therefore, the ground validation samples were sufficient and scale-matched. 2) In terms of model construction, the traditional quadrat scale (0.25 m$^2$) was successfully upscaled to the MODIS pixel scale (6,2500 m$^2$) based on the random forest and stepwise upscaling methods. Compared with previous studies, the scale matching of independent and dependent variables was achieved, effectively reducing the impact of spatial scale mismatch. The results showed that the correlation between the AGB values estimated by UAV and MODIS vegetation indices was higher than that between field measured AGB and MODIS vegetation indices at the MODIS pixel scale. The multi-year validation results showed that the constructed MODIS pixel scale AGB estimation model had good robustness, with an average $R^2$ of 0.83 and RMSE of 34.13 g·m$^{-2}$. Our dataset provides an important input parameter for a comprehensive understanding of the role of the QTP under global climate change. The dataset is available from the National Tibetan Plateau/Third Pole Environment Data Center (https://doi.org/10.11888/Terre.tpdc.272587, Zhang et al., 2022).

## 1 Introduction

Grasslands, accounting for approximately 37% of the earth's surface, play an essential role in the global carbon cycle and food supply (Ómara, 2012). However, most natural grasslands have been degraded to a certain extent due to overgrazing, farmland encroachment, soil erosion, and global climate change (Suttie et al., 2005; Ramankutty et al., 2008; Ómara, 2012). Therefore, timely monitoring of grassland health is crucial for the sustainable development of livestock and understanding of the global carbon cycle. Aboveground biomass (AGB) is a key indicator of grassland status and an important input parameter for ecological modeling and carbon storage estimation. Thus, accurate and rapid estimation of AGB is valuable for grassland monitoring.

The advent of satellites has made it possible to map the spatiotemporal dynamics of grasslands over large areas. Spectral information from different satellite sensors has been employed for biomass estimation, such as Sentinel-2, Landsat, and MODIS (Wang et al., 2019; Zhang et al., 2016). Although there are differences in spatial and spectral resolution, the core idea of the biomass estimation model is to construct linear or nonlinear relationships between the field-measured samples and various satellite spectral indices. Therefore, the accuracy of the estimation is closely related to the quality and quantity of ground samples (Morais et al., 2021; Yu et al., 2021). However, there are still two deficiencies in ground data acquisition: the large spatial gap between the traditional samples and satellite pixels, and the low efficiency.

How to narrow the spatial gap between traditional samples and satellite pixels is an urgent problem to be solved. Since it is impossible to harvest all grasses within a satellite pixel range, the average of 3-5 quadrats (0.5 m × 0.5 m or 1 m × 1 m) is usually used as the measurement (Dusseux et al., 2015; Yang et al., 2017), which results in a considerable spatial gap. A lot of studies have been carried out to upscale ground measurements to satellite pixels (Crow et al., 2012; Bian and Walsh, 1993), such as block Kriging geostatistical interpolation, different types of regression models, and machine learning algorithms (Cheng et al., 2007; Wang et al., 2014; Cannavacciuolo et al., 1998; Dancy et al., 1986; Li et al., 2018). However, the accuracy of these methods depends on the density of sampling points. In addition, fine-resolution satellite images were used as a bridge to reduce the impact of scale mismatch on AGB estimation (Yu et al., 2021; He et al., 2019). The rationale is that the finer the resolution of satellite image, the smaller the spatial gap with the ground samples (Wang and Sun, 2014; Morais et al., 2021). Therefore, filling the spatial gap between ground samples and satellite pixels is the key to improving the accuracy of satellited AGB estimation.

Improving the efficiency of ground sampling is another issue that needs to be addressed. Although the traditional sampling method can yield high-accuracy results, it is time-consuming and labor-intensive. For example, five years were spent in completing the collection of ground samples to map the grassland AGB in China (Yang et al., 2010). Moreover, with limited original ground data, some scholars had to use the data published by others to increase the sample amount (Xia et al., 2018;

67  Jiao et al., 2017). However, datasets from different sources may affect the overall accuracy due to the differences in quadrat

68  size, plot size, and harvesting methods.

69

70  As a linkage/bridge between field observation and satellites detecting for grassland biomass, the development and popularity

71  of unmanned aerial vehicle (UAV) technology has provided a new solution to the abovementioned two issues. UAV

72  photograph has been successfully used to estimate ecological metrics such as fractional vegetation cover (FVC), biomass,

73  and canopy height (Chen et al., 2016; Zhang et al., 2018; Bendig et al., 2015). The use of UAVs has the following two

74  unparalleled advantages over traditional sampling methods. First, UAVs can effectively obtain two- or three-dimensional

75  vegetation information in a non-destructive way, which is helpful for grassland monitoring (Lussem et al., 2019; Zhang et al.,

76  2022a; Zhang et al., 2018). Second, UAVs can rapidly collect key parameters of grassland within satellite pixels (e.g., FVC,

77  Chen et al. 2016). Hence, UAV photographs can serve as a bridge to fill the spatial gap between field samples and satellite

78  pixels. However, most current UAV-based grassland biomass estimations are conducted on a small scale, but few studies are

79  on a regional scale. Whether UAVs can be used to fill the spatial gap between traditional ground sampling and satellite

80  pixels remains an open question. In addition, there is a shortage of multi-year validation to test the robustness of the AGB

81  estimation model over time due to the limited sample amount in previous studies.

82

83  This study proposed a new approach combining traditional ground sampling, UAV photograph, and satellite image to

84  produce a new reliable AGB dataset for the grasslands of the Qinghai-Tibetan Plateau (QTP). The objectives of this study

85  were: 1) to construct a UAV-based grassland AGB estimation model at the quadrat/MODIS pixel scales, respectively; 2) to

86  investigate whether UAVs can be used as a bridge to fill the spatial gap between ground samples and satellite pixels to

87  improve the accuracy of grassland AGB estimation, and 3) to map the AGB of alpine grasslands on the QTP from 2000 to

88  2019.


89  **2 Materials and Methods**

90  **2.1 Study Site**

91  QTP is the highest and largest plateau on the earth ($26°00′12″\sim39°46′50″$N, $73°18′52″\sim104°46′59″$E), with an average

92  elevation of ~4000 m and an area of approximately $257.24 \times 10^4$ km$^2$ (Figure 1). It is located in western China, with an

93  average annual temperature and precipitation of about 1.6°C and 413.6 mm, respectively. The primary grassland types are

94  meadow, steppe, and desert, which play a critical role in climate regulation, water conservation, and biodiversity protection

95  (Ding et al., 2013). In this study, the boundary of the QTP (Zhang et al., 2014) was downloaded from the National Earth

96  System Science Data Center, National Science & Technology Infrastructure of China (http://www.geodata.cn). Grassland

97  types were derived from the 1: 1000000 Chinese digital grassland classification map provided by the China Resource and

98  Environmental Science and Data Center (https://www.resdc.cn/). This dataset, generated through field surveys in the 1980s

99    and supplemented by satellite and aerial imagery, is the most detailed grassland-type map available. To facilitate comparison

100   with others' AGB estimates, we regrouped the grassland types into three categories: meadow, steppe, and desert (Table A1),

101   and resampled this regrouped vector to a grid with 250 m spatial resolution.
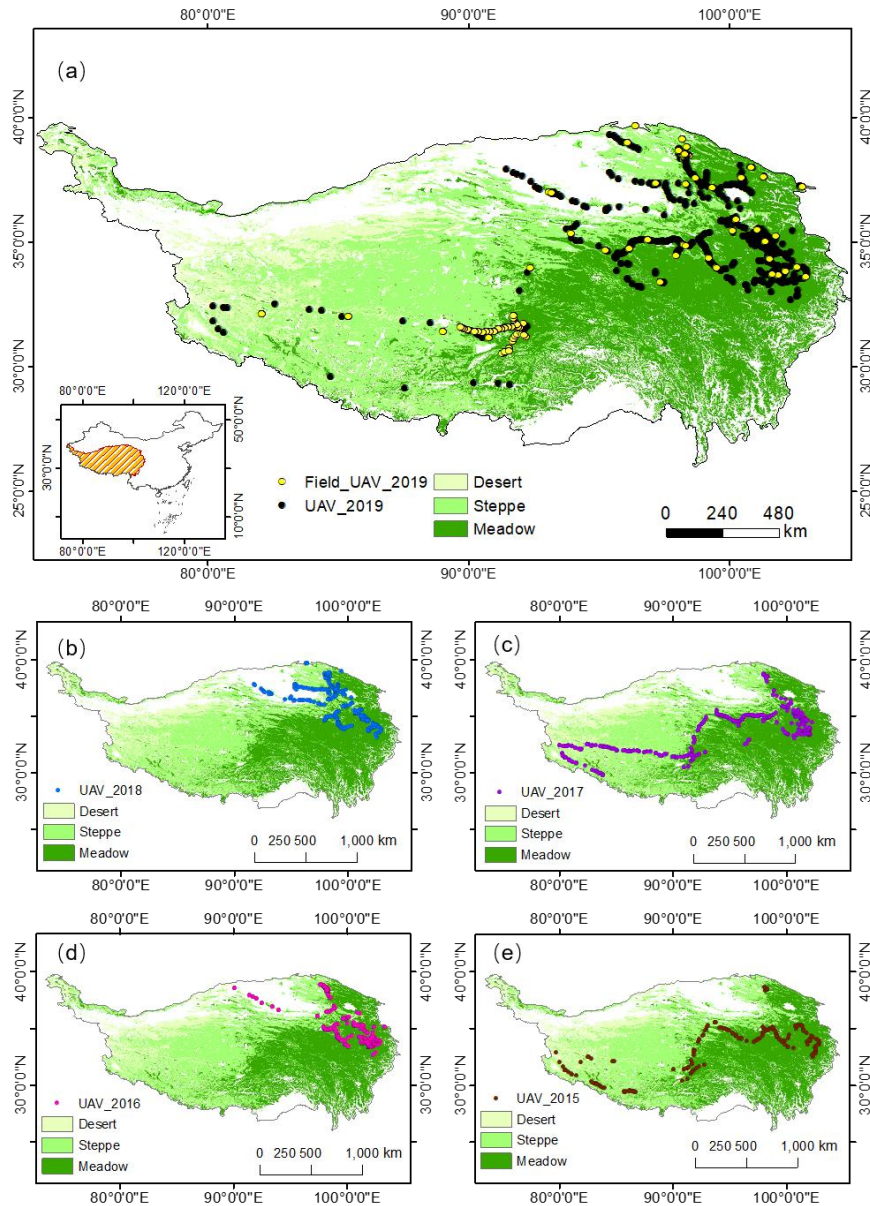


102

103   **Figure 1. Distribution of field and UAV sampling sites in 2019 (a); UAV sampling sites in grasslands on the QTP from 2015-2018**

104   **(b-e). Field_UAV_2019 represents the quadrat-scale sampling sites for the 2019 UAV-Field synchronous grassland biomass**

105   **experiment. UAV_year represents the UAV sampling points based on the GRID or RECTANGE mode of the corresponding year.**

106 **2.2 Overall technology roadmap**

107 The overall flowchart of this study is shown in Figure 2. It consisted of four main steps: 1) UAV and field investigation; 2)

108 constructing the AGB estimation model at the quadrat scale; 3) upscaling the grassland AGB to the MODIS pixel scale (250

109 m); 4) building the AGB estimation model at the MODIS pixel scale (250 m) and applying it to the QTP region. More

110 detailed information about each step was described in the following sections.
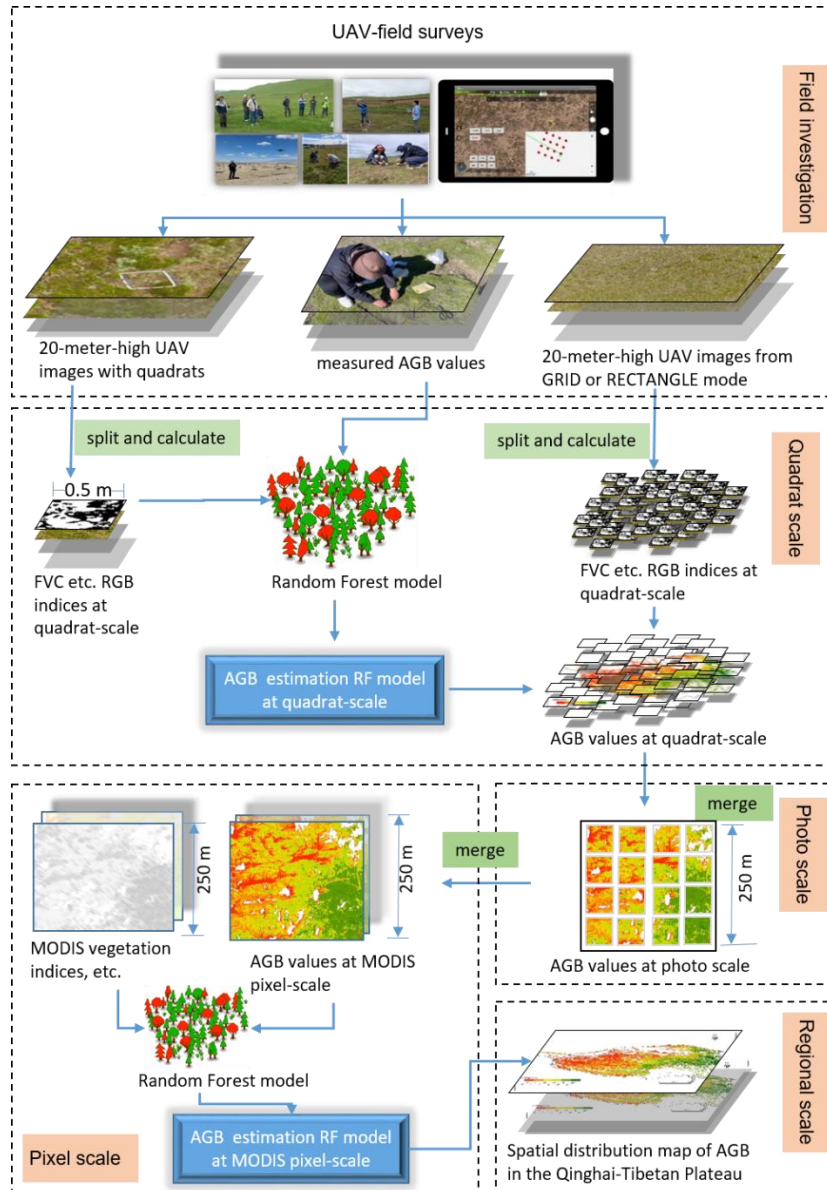


111
112
113 **Figure 2. The overall flowchart of UAV field survey and the construction of grassland AGB estimation models at different spatial**
114 **scales.**

5

## 2.3 Field investigation

### 2.3.1 UAV and route planning

DJI Phantom 3 Professional (DJI Company, Shenzhen, China), a popular consumer quadrotor UAV with a high-resolution RGB camera, was used to collect UAV photos of the QTP from 2015 to 2019. It has a 1/23-inch CMOS sensor and is capable of taking 12-megapixel photos. In addition, it uses a 3-axis stable gimbal to take photos vertically downward to eliminate the distortion of UAV photos. It has good environmental adaptability, with an operating temperature range from 0°C to 40°C, and a maximum take-off altitude of 6000 m. Therefore, DJI Phantom 3 Professional is adequate to monitor grassland states on the QTP. More detailed information about the UAV system was listed in Table A2.

Fragmentation monitoring and analysis with aerial photography (FragMap) system was used for UAV route planning (Yi, 2017). During 2015-2019, we conducted UAV monitoring of the QTP grasslands using FragMap (Figure 1). Over 2,000 fixed flight routes were set up during this period, and more than 40,000 UAV photos were collected, providing a sufficient dataset for this study (Table 1).

**Table 1. UAV sampling information from 2015 to 2019**

| Year | Flight Mode | Number of route | Photo number | Acquisition date |
|------|-------------|-----------------|--------------|------------------|
| 2015 | RECTANGLE | 214 | 2568 | 7/05 ~ 8/24 |
| 2016 | RECTANGLE | 334 | 4008 | 6/20 ~ 9/29 |
|      | GRID | 150 | 2400 | 6/20 ~ 9/23 |
| 2017 | RECTANGLE | 315 | 3780 | 5/10 ~ 10/24 |
|      | GRID | 322 | 5152 | 7/15 ~ 8/22 |
| 2018 | RECTANGLE | 79 | 948 | 7/22 ~ 8/03 |
|      | GRID | 303 | 4848 | 7/04 ~ 8/29 |
| 2019 | GRID | 885 | 14160 | 7/12 ~ 9/21 |
|      | BELT | 151 | 2416 | 7/12 ~ 9/21 |
| **Total** | | **2753** | **40280** | |

GRID, RECTANGLE, and BELT are the most widely used flight modes in FragMap software. Among these modes, GRID and RECTANGLE modes have 16 and 12 waypoints for capturing UAV photos within a MODIS pixel range (250 m × 250 m) (Figure A1). The flying height and speed are set to 20 m and 3 m/s, respectively. The spatial coverage area of a 20-meter-high UAV photo is about 26 m × 35 m. The BELT mode is similar to GRID, but is designed to obtain near-ground UAV

135  photos with higher resolution (Figure 3b). Normally, the BELT size is set to 40 m × 40 m, and the flying height and speed

136  are set to 2 m and 1 m/s to ensure that field crews have enough time to place sampling quadrats under the UAV waypoints.

137  Therefore, it can be used to help field workers quickly and evenly place sampling quadrats. As with the GRID mode, 16

138  UAV photos can be captured in a single flight of BELT. Compared with the MOSAIC mode (which requires a guaranteed

139  overlap rate between photos to obtain a full view of an area), our design is more in line with the traditional ecological

140  sampling concept and more conducive to rapid sample collection.
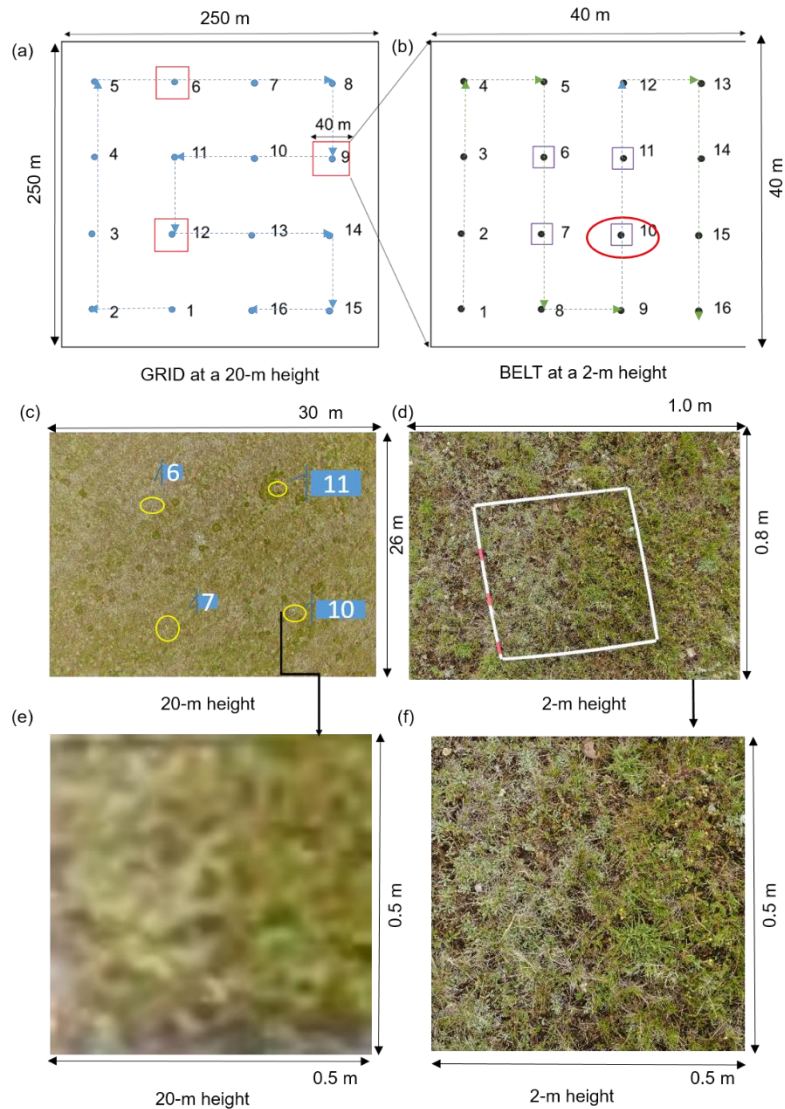


141

142  **Figure 3. Schematic diagram of the UAV-field synchronization experiment in 2019: a combination design of GRID (a) and BELT**

143  **(b) flight modes; a UAV photo with a quadrat from the BELT mode at the height of 2 m (d); a 20-meter-high UAV photo including**

144  **four sample quadrats (c); and the cropped UAV photos at the quadrat scale from 20 m (e) and 2 m (f) height, respectively.**

7

145 **2.3.2 Synchronization experiment of UAV and field sampling**

146 A UAV-field biomass synchronization experiment was conducted in 2019 to ensure spatial matching among satellites, UAVs,

147 and ground sampling (Figure 3). The specific four steps were as follows. Firstly, we set a GRID flight mode with a MODIS

148 pixel size (250 m × 250 m) (Figure 3a). Secondly, three waypoints were selected from the GRID flight mode  to set the

149 BELT flight modes (40 m × 40 m). For each BELT, a sampling quadrat (0.5 m × 0.5 m) was placed at its 6, 7, 10, and 11

150 waypoints to ensure that the GRID photo could contain the four abovementioned quadrats (Figure 3b-c). Thirdly, after the

151 implementation of all fights, the grassland samples were cut, bagged, and numbered. Finally, these samples were oven-dried

152 at 65℃ to constant weight to obtain the field-measured AGB values.

153

154 **2.4 Data processing**

155 **2.4.1 UAV photo pre-processing and indices calculation**

156 Pre-processing of UAV photos included image quality inspection, cropping, and calculation of different indices. It should be

157 noted that only UAV photos at 20 m height were used in this paper. Firstly, we eliminated overexposed or blurred 20-meter-

158 high UAV photos. Secondly, the pixels in the sampling quadrats were cropped and saved (Figure 3e). Thirdly, the RGB

159 indices, including color space, histogram, and vegetation indices, were calculated based on the method in our previous study

160 (Zhang et al., 2022a). In addition, 30 other RGB indices were added as candidate independent variables. The names,

161 formulas, and references of the above indices are shown in Table A3.

162 **2.4.2 MODIS vegetation index and other spatial data**

163 The MOD13Q1(v006) product was downloaded from the National Aeronautics and Space Administration (NASA) earth

164 explorer website (https://earthexplorer.usgs.gov/) for detecting the alpine grassland AGB on the QTP. The data contained

165 two commonly used vegetation indices, the Normalized Vegetation Index (NDVI) and the Enhanced Vegetation Index (EVI),

166 with spatial and temporal resolutions of 250 m and 16 days, respectively. A total of 2,842 scenes from 2000 to 2019 were

167 downloaded. Then, the MODIS images were reprojected and mosaiced using the MODIS Projection Tool (MRT). After that,

168 the corresponding vegetation indices closest to the date of the UAV sampling were extracted to construct/validate the

169 MODIS pixel-scale AGB estimation model. In addition, the kNDVI was calculated to overcome the NDVI saturation issue

170 based on the equation $kNDVI = TANH (NDVI^2)$ (Camps-Valls et al., 2021). The annual maximum vegetation indices were

171 calculated by the maximum value composition (MVC) algorithm to estimate the spatial AGB distribution of the QTP from

172 2000 to 2019 (Holben, 1986; Wang et al., 2021; Gao et al., 2020).

173

174 Furthermore, meteorological, soil texture, and topographic data were included as candidate independent variables for

175 constructing the MODIS pixel-scale AGB estimation model. Meteorological factors, including mean annual temperature

8

176 (MAT), mean annual precipitation (MAP), and total annual solar radiation (TASR), were calculated based on the daily
177 meteorological dataset from the National Meteorological Information Center of China (http://data.cma.cn/). The data
178 processing steps mainly included checking and eliminating the anomalous values of attributes, cumulative summation,
179 annual averaging, and interpolation to obtain a meteorological raster dataset with a spatial resolution of 1 km (Li et al., 2021).
180 Moreover, soil texture data at 1 km spatial resolution, including the ratio of soil organic matter (SOM), clay, sand, and silt,
181 were downloaded from the Resource and Science and Data Center of China (https://www.resdc.cn/). All the meteorological
182 and soil raster datasets were regridded into 250 m by ArcGIS software (Version 10.2, Environmental Systems Research
183 Institute, Inc.) to match the MODIS image.
184
185 Terrain factors including altitude, slope, and aspect, were derived from the digital elevation model (DEM) using the terrain
186 analysis tool of ArcGIS software. The DEM was retrieved from Shuttle Radar Topography Mission (SRTM) imagery
187 (version 004, 90 m) and regridded to 250 m.

188 **2.5 AGB modeling and computation at different scales**

189 We estimated the grassland AGB at three scales: the quadrat scale, the photo scale, and the MODIS pixel scale (Figure 4).
190 More detailed information was described as follows.
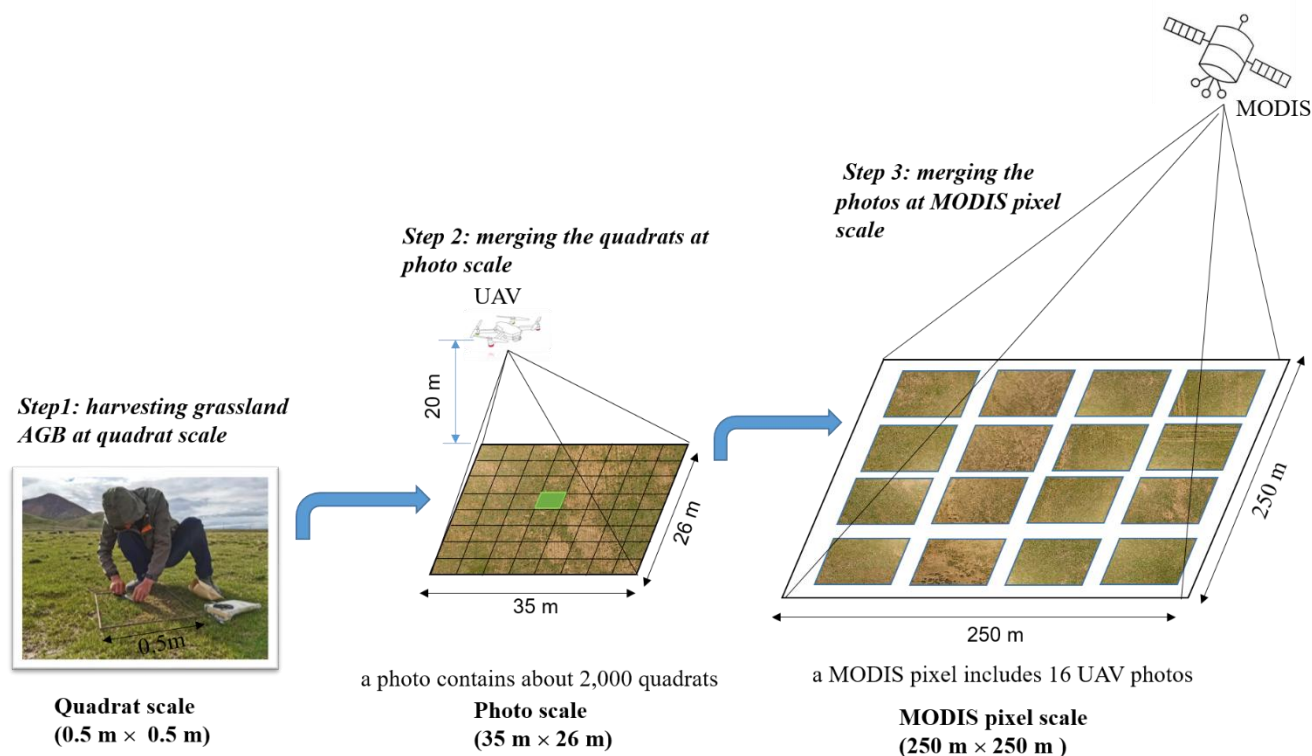


191
192    **Figure 4. Upscaling steps to estimate grassland AGB matching the MODIS pixel scale.**

### 2.5.1 Random forest model

Random Forest (RF) (Breiman, 2001) is an ensemble-learning algorithm that has been widely used to estimate AGB due to its excellent performance (Ghosh and Behera, 2018; Mutanga et al., 2012; Wang et al., 2016). The two primary parameters, named the number of regression trees in the forest *(ntree)* and the number of feature variables required to create branches *(mtry)*, were firstly optimized based on the root mean square error (RMSE) of training data. Here, the value of *ntree* was set from 100 to 5000 with an interval of 100, while *mtry* was set as the square root of the number of training sample features. In addition, the importance of each predictor was ranked by calculating the percentage increased in mean square error (%IncMSE).

The backward feature elimination method (BFE) was used to reduce the number of input variables to simplify the RF model (Vergara and Estévez, 2014). The primary steps were as follows: 1) constructing an AGB RF model by including all predictors in the initial stages and calculating the %IncMSE for each variable; 2) eliminating the least promising variable and then rerunning the RF model until only one independent variable was left. Moreover, the corresponding coefficient of determination ($R^2$) and the corresponding RMSE were calculated in each iteration; 3) the smallest subset of variables with the highest $R^2$ was selected as the final optimized indices.

In addition, different training and validation strategies were used at different scales. A 10-fold cross-validation method was used at the quadrat scale due to the limited ground samples (Kohavi, 1995). At the MODIS pixel scale, 30% of the UAV-estimated AGB samples in 2019 were randomly selected as an independent validation dataset due to its large size. Meanwhile, the UAV_AGB values from 2015 to 2018 were used for multi-year validation to test the robustness of the model over time. Statistical metrics $R^2$ (Eq.1) and RMSE (Eq.2) were used to evaluate model performance.

$$R^2 = 1 - \frac{\sum_{i=1}^{n}(\hat{y}_i - y_i)^2}{\sum_{i=1}^{n}(\hat{y}_i - \bar{y}_i)^2} \tag{1}$$

$$RMSE = \sqrt{\frac{\sum_{i=1}^{n}(\hat{y}_i - y_i)^2}{n}} \tag{2}$$

where n is the number of samples, $y_i$ and $\hat{y}_i$ represent the measured and the predicted AGB value, respectively, $\bar{y}$ is the mean value of measured AGB samples.

### 2.5.2 AGB RF estimation model at the quadrat scale (0.25 m²)

Since the spatial coverage area of a 20-meter-high UAV photo (26 m × 35 m) is much larger than a single 2-meter-high UAV photo (0.8 m × 1 m), making it easier to match the MODIS pixel scale (250 m × 250 m). Hence, the 20-meter-high UAV photos containing the sample quadrats were chosen for constructing the quadrat-scale AGB estimation model. A total of 906 pairs between field harvested AGB and UAV sub-photos were collected, with good spatial representativeness (Figure 1a, yellow dots). The observed AGB values ranged from 0 to 450 g·m⁻², with mean and median values of 59.75 g·m⁻² and

224  33.04 g·m⁻², respectively (Figure 5a). The cropped 20-meter-high UAV photo indices and the measured AGB values were
225  used as the independent and dependent variables to build the RF model at the quadrat scale (Figure 2).

### 2.5.3 AGB calculation at the photo scale (~900 m²)

227  The steps for AGB estimation of the whole 20-meter-high UAV photo were as follows: 1) Firstly, each UAV photo was split
228  into ~2,000 quadrat-sized small patches. 2) Secondly, the AGB of each small patch was calculated based on the quadrat-
229  scale AGB estimation model. 3) Finally, the average of all small patches was calculated as the AGB of the whole photo.
230  Based on the above steps, the AGB values of more than 75 million quadrats in 37,864 photos in GRID or Rectangle mode
231  were calculated (Table 1).

232
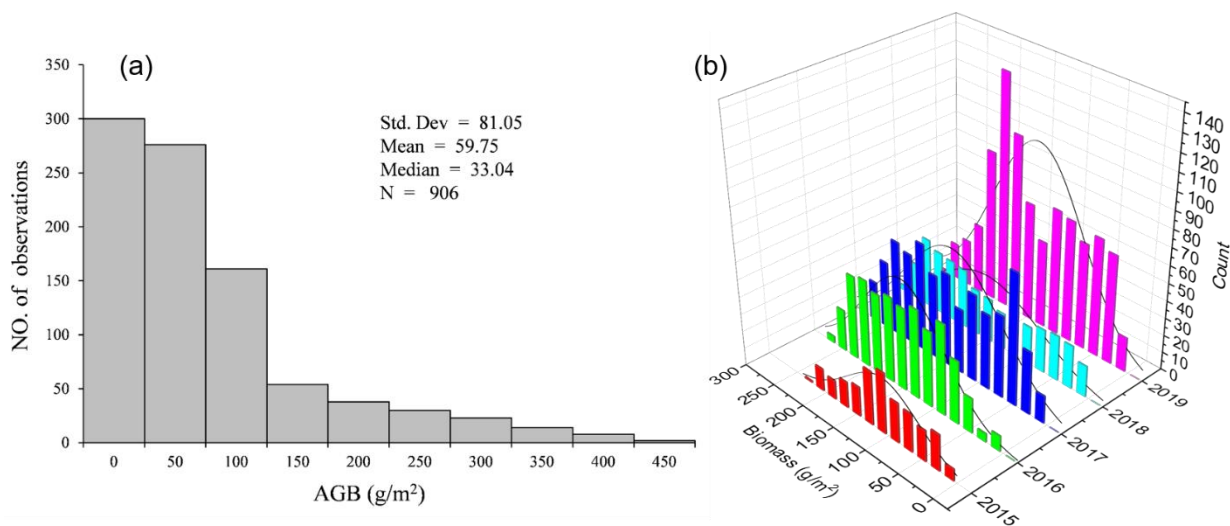


**Figure 5. Histograms of field-measured AGB values at quadrat scale (a) and UAV-estimated AGB values of different years at the photo scale (b).**

236

### 2.5.4 AGB RF model construction at MODIS pixel-scale (6,2500 m²)

238  The following steps were involved in constructing the AGB estimation model at the MODIS pixel scale. 1) Since the
239  coverage area of a GRID or RECTANGLE mode was similar to that of a MODIS pixel, the average value of 16 or 12 UVA
240  photos' AGB was taken as the AGB value of the corresponding MODIS pixel. During 2015-2019, a total of 2,602 UAV-
241  estimated AGB samples were obtained at the MODIS pixel scale (Table 1). 2) The MODIS vegetation indices and other
242  spatial metrics (such as meteorological, soil texture, and topographic data) corresponding to each GRID or RECTANGLE
243  mode were then extracted using the ArcGIS software. Here, the MODIS NDVI, EVI, and kNDVI indices closest to the

244 sampling date were chosen to minimize the time difference between sampling and satellite overpass. 3) Subsequently, the
245 UAV-estimated AGB values, MODIS vegetation indices, and other spatial metrics were used as dependent and independent
246 variables to build the AGB estimated model at MODIS pixel scale using the RF model.

**2.6 Uncertainty analysis**

248 Since the actual AGB values of MODIS pixels cannot be directly obtained, the regression coefficient between vegetation
249 indices and estimated AGB was used to quantify the uncertainty of different AGB estimation methods. In other words, the
250 higher the correlation between the estimated AGB and MODIS vegetation indices, the more accurate the estimation model
251 was. The performance of the estimation model was evaluated through three aspects. In this study, we first compared the
252 correlation between the MODIS vegetation indices and AGB values obtained by traditional sampling and UAV estimation
253 methods. We also explored the uncertainties of UAV sampling coverage area by regularly combining the number of photos
254 in a MODIS pixel, and tested whether the estimated AGB was closer to the "true" value as the number increased.
255 Furthermore, the AGB validation results between GRID and RECTANGLE at the pixel scale were compared to understand
256 the uncertainties caused by different flight modes.

**2.7 Trend analysis of grassland AGB**

258 This study combined the Theil-Sen median trend analysis and Mann-Kendall test to analyze the temporal variation
259 characteristics of grassland AGB in QTP (Jiang et al., 2015). Theil-Sen median trend analysis is a robust trend statistical
260 method with high computational efficiency, insensitive to outliers (Hoaglin et al., 1983). The Mann-Kendall test is a
261 nonparametric test for time series trends, which does not require the measurements to follow a normal distribution and is not
262 affected by missing values and outliers. The Theil-Sen Median trend analysis and Mann-Kendall trend test have been widely
263 used to analyze the temporal trend of vegetation index, cover, and biomass (Gao et al., 2020; Jiang et al., 2015; Fensholt et
264 al., 2009). The detailed formulas for the Theil-Sen median trend analysis and the Mann-Kendall method are provided by
265 Jiang et al. (2015).

**3 Results**

**3.1 Independent variables selected for AGB modeling**

268 The independent variables for AGB estimation at the quadrat and MODIS pixel scales were presented in Table 2. A total of
269 36 independent variables were selected at the quadrat scale, including 26 vegetation RGB indices, six histogram indices, and
270 four color space indices (Figure A2). At the MODIS pixel scale, five variables were selected, including NDVI, kNDVI, EVI,
271 MAP, and DEM (Figure A3).
272
273

Table 2. Selected independent variables for the AGB modeling at quadrat and pixel scales. The full names of each variable at the quadrat scale were listed in Table A3.

| Scale | Model | Number | Independent variables |
|---|---|---|---|
| Quadrat | $RF_Q$ | 36 | FVC, WI, GI, EXG, TGI, EXGR,VEG, GRATIO, COM, CIVE, RGBVI, EXR, GLA, GRRI, MVARI, MGRVI, GRVI, RGRI, GBRI, VARI, NDI, RRATIO, EXB, V, IPCA, INT, HOC_R_CORR, HOC_B_CHIS, HOC_R_CHIS, HOC_G_CHIS, HOC_G_CORR, HOC_B_CORR，B, H, G, R |
| Pixel | $RF_P$ | 5 | NDVI, kNDVI, EVI, DEM, MAP |

## 3.2 Modeling and accuracy assessment

For the AGB estimation model at the quadrat scale, the results of 10-cross validations showed that there was a significant linear relationship between the estimated and the field measured values ($R^2 = 0.73$, $p < 0.001$, Table 3, Table A4). There was no significant difference ($p > 0.05$) between the predicted and the measured values of the mean AGB at a confidence level of 95% (Table 4) with an RMSE of 32.94 g·m$^{-2}$ (Table 3). The model predicted well when the measured biomass was less than 150 g·m$^{-2}$, however, underestimation was found when the measured biomass was more than 200 g·m$^{-2}$ (Figure 6a). It may be because the number of samples more than 200g/m$^2$ is relatively small, accounting for only 8.50% of all samples (Figure 5a). Although the sample amount of UAV varied year by year, the AGB values estimated from UAV photos typically ranged from 0 to 300 g·m$^{-2}$ (Figure 5b).

For the AGB estimation model at the MODIS pixel scale, there was a strong linear relationship ($p < 0.05$) between the estimated AGB and that measured by UAV photos for 2015-2019 (Table A4). The fitting coefficient $R^2$ was 0.85 for 2017-2019, and slightly lower for 2015-2016 with the value of 0.63 and 0.77, respectively (Table 3, Figure 6b-f). The RMSE of the pixel-scale model ranged from 23.36 to 34.07 g·m$^{-2}$ (Table 3). In addition, we found no significant differences ($p > 0.05$) between the predicted and measured values of the average AGB, except for 2017 and 2018 (Table 4). The average AGB estimated by the MODIS pixel-scale model for 2017 and 2018 were 131.48 g·m$^{-2}$ and 120.60 g·m$^{-2}$, which were 14.72% and 13.78% lower than those estimated by UAV photos. Although the average AGB estimates between the MODIS pixel-scale model and UAV were different in 2017 and 2018, the error percentages were acceptable. Therefore, the constructed MODIS pixel-scale AGB estimation model had good performance and robustness in different years (Figure 6b-f).

Table 3. Validation results of AGB models at the quadrat and pixel scales

| Scale | Year | Training set | | Validation set | |
|---|---|---|---|---|---|
| | | R² | RMSE(g·m⁻²) | R² | RMSE(g·m⁻²) |
| Quadrat-scale | 2019 | 0.94 | 20.18 | 0.73 *** | 32.94 |
| Pixel-scale | 2019 | 0.96 | 10.68 | 0.85 *** | 23.36 |
| | 2018 | — | — | 0.85 *** | 24.83 |
| | 2017 | — | — | 0.85 *** | 23.83 |
| | 2016 | — | — | 0.77 *** | 31.28 |
| | 2015 | — | — | 0.63 *** | 34.07 |

'***' significant at p < 0.001

Table 4. T-test results between the predicted and measured AGB values for the modes at the quadrat and pixel scales

| Validation model | Measured mean (g·m⁻²) | Predicted mean (g·m⁻²) | t | df | p-value |
|---|---|---|---|---|---|
| 2019_Quadrat-scale | 51.57 | 54.35 | -0.66 | 939.35 | 0.51 |
| 2019_Pixel_scale | 136.68 | 137.75 | -0.15 | 340.78 | 0.88 |
| 2018_Pixel_scale | 152.49 | 131.48 | 4.01 | 723.81 | 6.63e-05 |
| 2017_Pixel_scale | 141.42 | 120.60 | 5.48 | 1225.20 | 5.26e-08 |
| 2016_Pixel_scale | 149.56 | 142.70 | 1.68 | 961.99 | 0.09 |
| 2015_Pixel_scale | 108.65 | 98.23 | 1.96 | 1225.20 | 0.05 |

### 3.3 Correlation analysis between AGB values and MODIS indices

The correlations between the UAV-estimated AGB and MODIS vegetation indices were much better than that between field harvested AGB and MODIS vegetation indices (Figure 7a). For example, the correlation between NDVI and field harvested AGB was only 0.53, considerably lower than the correlation between NDVI and AGB obtained from a single UAV photo (r = 0.74). Moreover, the correlation between NDVI and UAV-estimated AGB increased with the increasing number of UAV photos. It increased rapidly as the number of UAV photos increased from 1 to 4 (from 0.74 to 0.86), then slowed down and stabilized (from 0.87 to 0.88). In addition, we compared the scatter plots and fitting lines between NDVI and different AGB estimation methods (Figure 7b-f). The results showed a weak linear relationship between the field-measured AGB and NDVI, with an $R^2$ of 0.29. While using the UAV sampling method, the linear relationship was greatly improved and increased with the increasing number of photos. The fit coefficient $R^2$ increased from 0.54 to 0.78, much higher than the traditional sampling method (Figure 7).
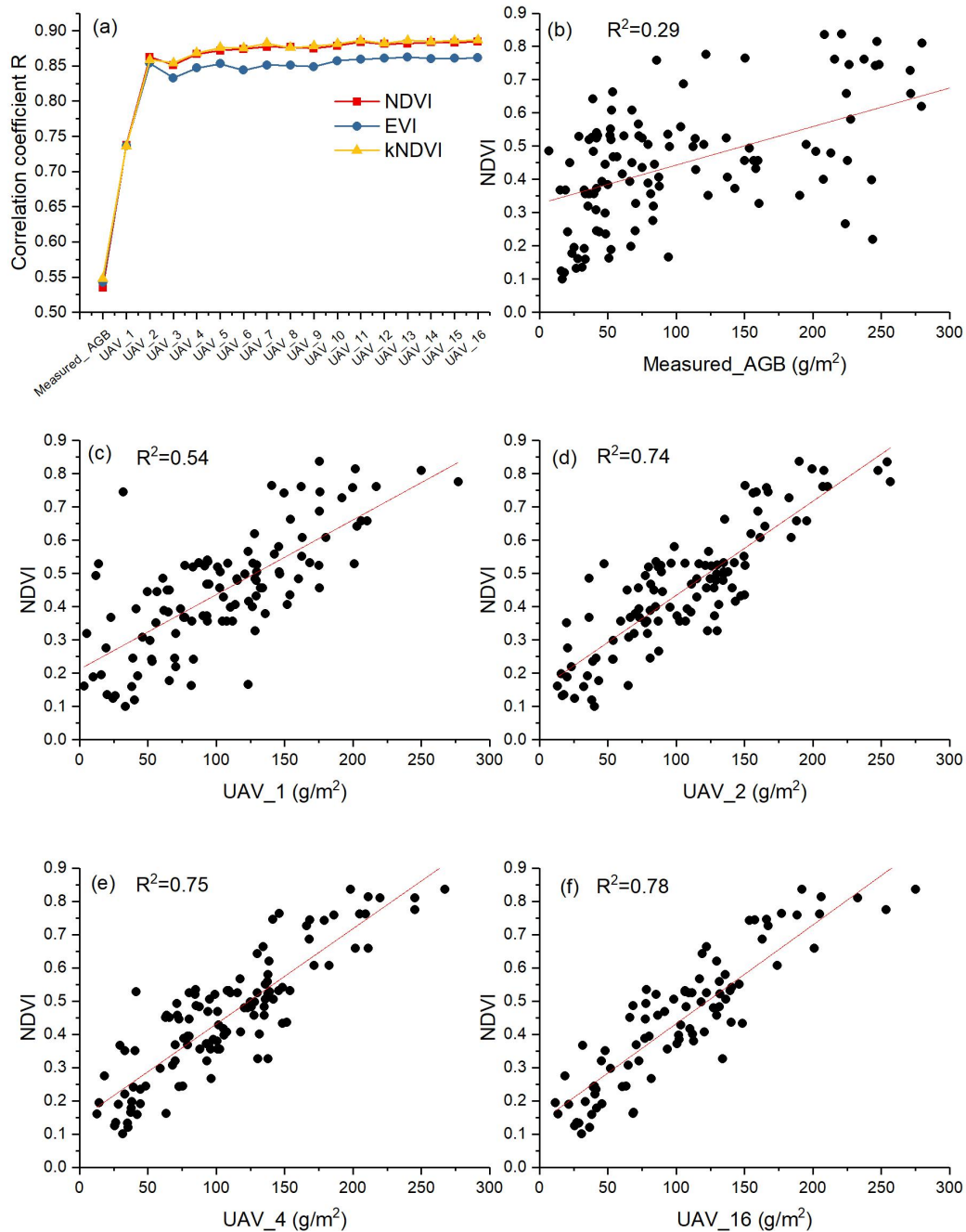
14
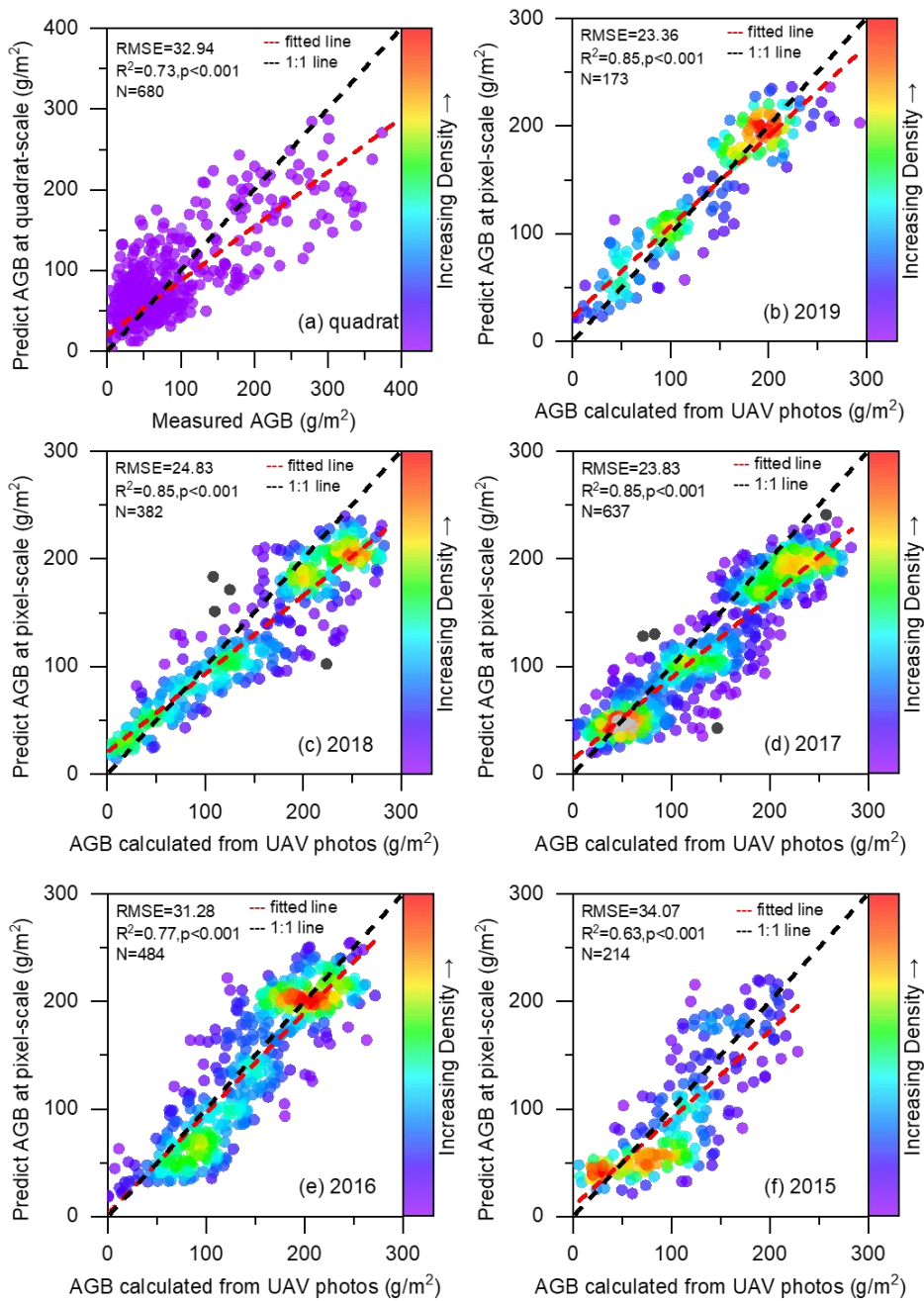
319
320
321 **Figure 6. Validation results of the AGB estimation models at the quadrat (a) and MODIS pixel scale for 2015-2019 (b-f).**

322

Figure 7. Correlation between MODIS vegetation indices and different AGB estimation methods (a); scatter plots of NDVI with different AGB estimation methods (b-f). UAV_x, x represents the number of UAV photos used to estimate the average AGB at the MODIS pixel scale. Here, x ranges from 1 to 16.

## 3.4 Spatial distribution of grassland AGB

The spatial distribution of the average grassland AGB on the QTP from 2000 to 2019 was calculated (Figure 8). The AGB gradually increased from west to east. The average AGB of eastern OA1, IIAB1, IB1, and IIC2 eco-geographical regions ranged from 150 to 190 $g \cdot m^{-2}$, and the average AGB of IC1 and IIC1 ranged from 80 to 110 $g \cdot m^{-2}$ (Figure 8b). The average AGB of IID2, IID3, IC2, and IID1 in the west was relatively low, ranging from 35 to 75 $g \cdot m^{-2}$. The ID1 region was dominated by desert grassland with the lowest average annual AGB values, which fluctuated around 20 $g \cdot m^{-2}$ (Figure 8b). Except for the low AGB due to low precipitation in 2015 (Figure A4), the mean AGB showed an overall increasing trend from 2000 to 2019, with an average growth rate of 0.22 $g \cdot m^{-2} \cdot a^{-1}$ (Figure 9a). The overall mean AGB of the QTP was 103.6 $g \cdot m^{-2}$, with 151.85 $g \cdot m^{-2}$, 60.85 $g \cdot m^{-2}$, and 28.91 $g \cdot m^{-2}$ for meadow, steppe, and desert grassland, respectively (Figure 9b). In addition, the temporal trend of grassland AGB in each pixel was analyzed. As shown in Figure 10, the IID3, ID1, IID2, and IIC2 eco-geographical regions of the northern QTP showed an increasing trend from 2000 to 2019, while the IC2, IB1, and IIC1 regions showed a decreasing trend. Therefore, there was spatial heterogeneity in the temporal variation.
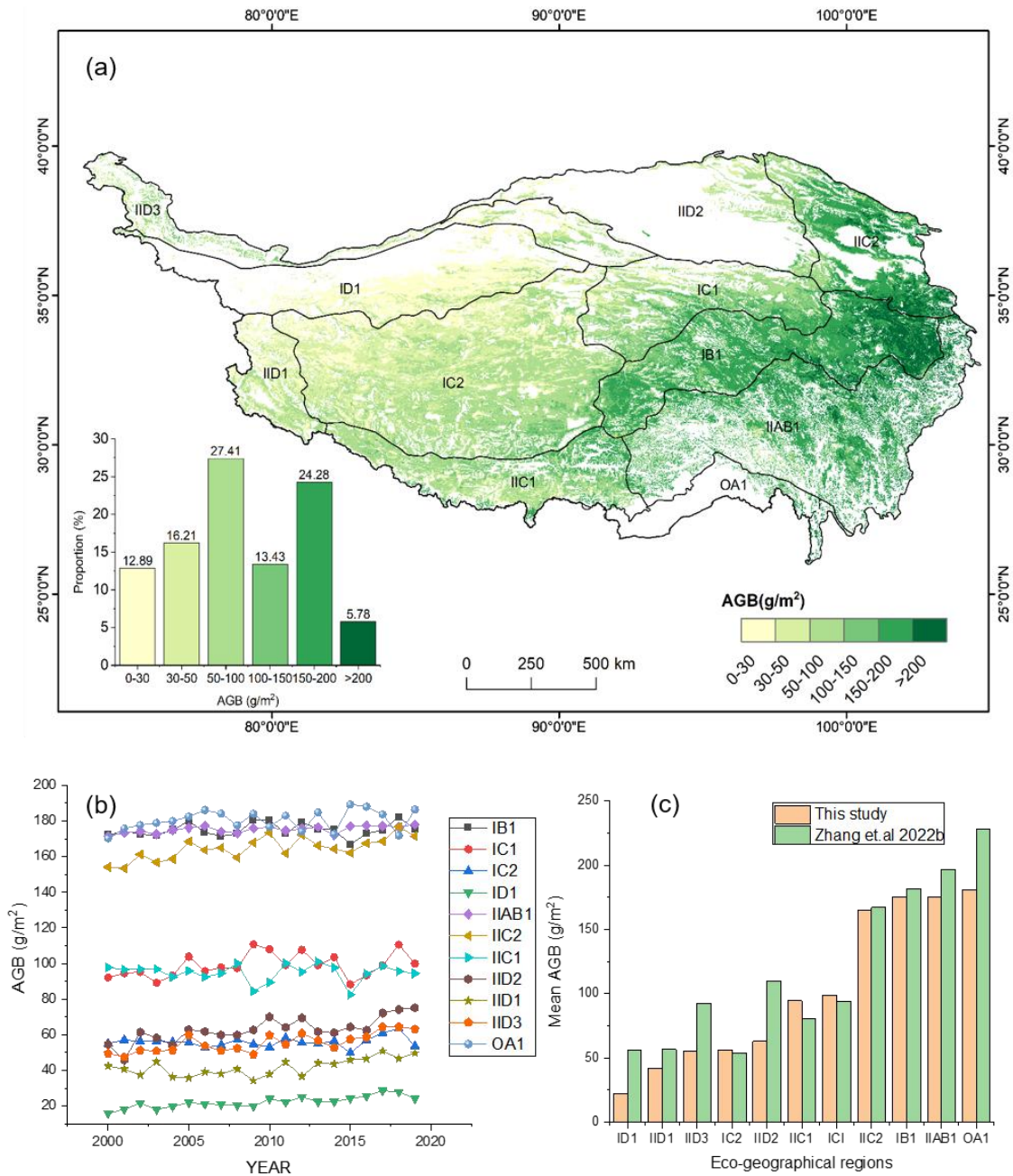
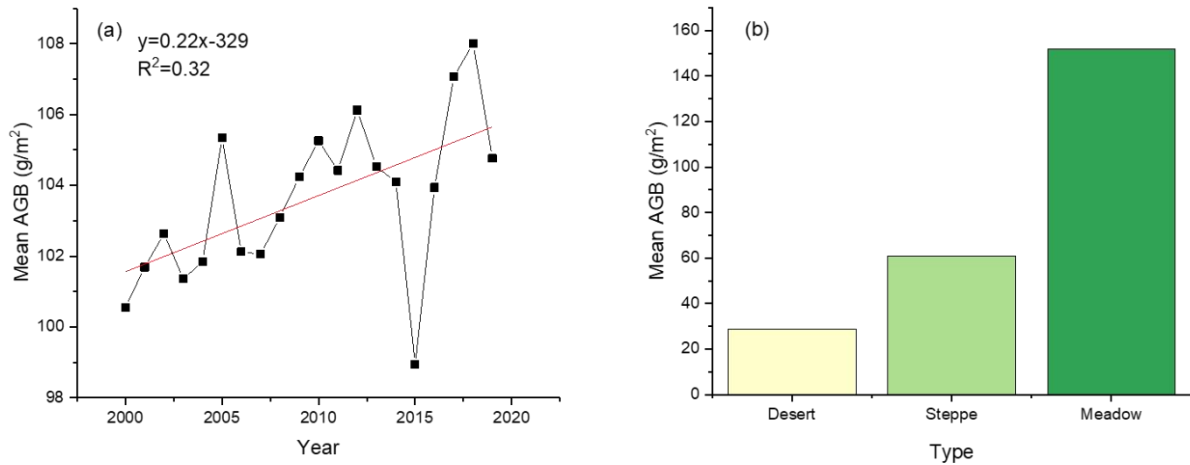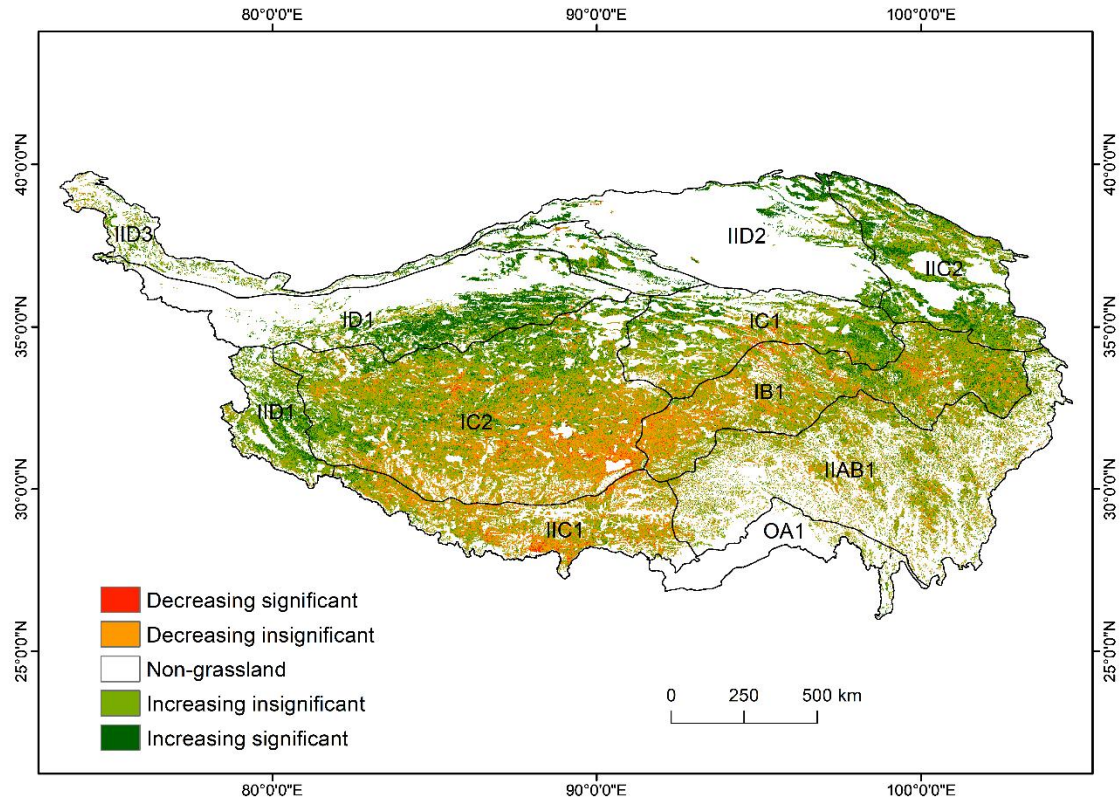Figure 8. (a) The spatial distribution of average grassland AGB on the QTP from 2000 to 2019. IID1, IID2, IID3, ID, IIC1, IIC2, IC1, IB1 IIAB1, and OA1 are the eco-geographical regions of the QTP(Zheng, 1996). The full names of each eco-geographical region were listed in Table A5. (b) AGB values of each eco-geographical region from 2000 to 2019. (c) Comparison of multi-year AGB averages in the different eco-geographical regions.

18

347

348 **Figure 9. Variation trend of average grassland AGB on the QTP from 2000 to 2019 (a) and average AGB of different grassland**
349 **types (b).**



350

351 **Figure 10. Spatial trends of grassland AGB on the QTP from 2000 to 2019. IID1, IID2, IID3, ID, IIC1, IIC2, IC1, IB1 IIAB1, and**
352 **OA1 are the eco-geographical regions of the QTP (Zheng, 1996). The full names of each eco-geographical region were listed in**
353 **Table A5.**

19

## 4 Discussion

### 4.1 Scale matching and its impact factor

In previous studies, the AGB values at the satellite pixel scale were usually represented by the average of 3-5 quadrat-scale samples placed in the corresponding satellite pixel, resulting in a large spatial gap between the ground samples and the satellite pixels (Yang et al., 2017; Yang et al., 2009; Meng et al., 2020). The spatial gap between ground samples and satellite pixels affects the accuracy of grassland AGB estimation models (Morais et al., 2021). Therefore, we used the UAVs as a bridge to fill the spatial gap. Spatial scale matching of dependent and independent variables was achieved in estimating AGB values at different scales. Firstly, at the quadrat scale, the independent variables were all derived from cropped 20-meter-high UAV photos corresponding to the ground samples (Figure 3e). Secondly, the 20-meter-high UAV photo was split into ~2000 quadrat-sized patches to ensure consistency with the quadrat-scale model, and the average of these patches was used as the final AGB at the photo scale. Finally, the AGB matching the MODIS pixel scale was calculated by averaging the AGB of 16 or 12 UAV photos within the MODIS pixel (Figure A1). With these three steps, we successfully upscaled the measured AGB from quadrat scale (0.5 m × 0.5 m) to photo scale (26 m × 35 m) and MODIS pixel scale (250 m × 250 m). Our results showed that the correlations between the UAV-estimated AGB values and the MODIS vegetation indices were higher than that between field harvested AGB and MODIS vegetation indices (Figure 7).

Furthermore, we found that the spatial coverage area of the UAV sampling had an impact on the scale matching. Our results showed that the closer the spatial coverage area of the UAV sampling was to the satellite pixel, the higher its correlation with MODIS vegetation indices (Figure 7a). It was further confirmed by comparing the validation results of different flight modes. At the MODIS pixel scale, we found that the $R^2$ between the model predictions and the AGB values estimated by GRID mode was better than that of RECTANGLE mode (Figure 11). The reason is that GIRD mode can take 16 photos within a MODIS pixel, while RECTANGLE mode can only take 12 photos (Figure A1). As a result, UAV photos could serve as a bridge to effectively fill the spatial gap between traditional samples and satellite data.

377
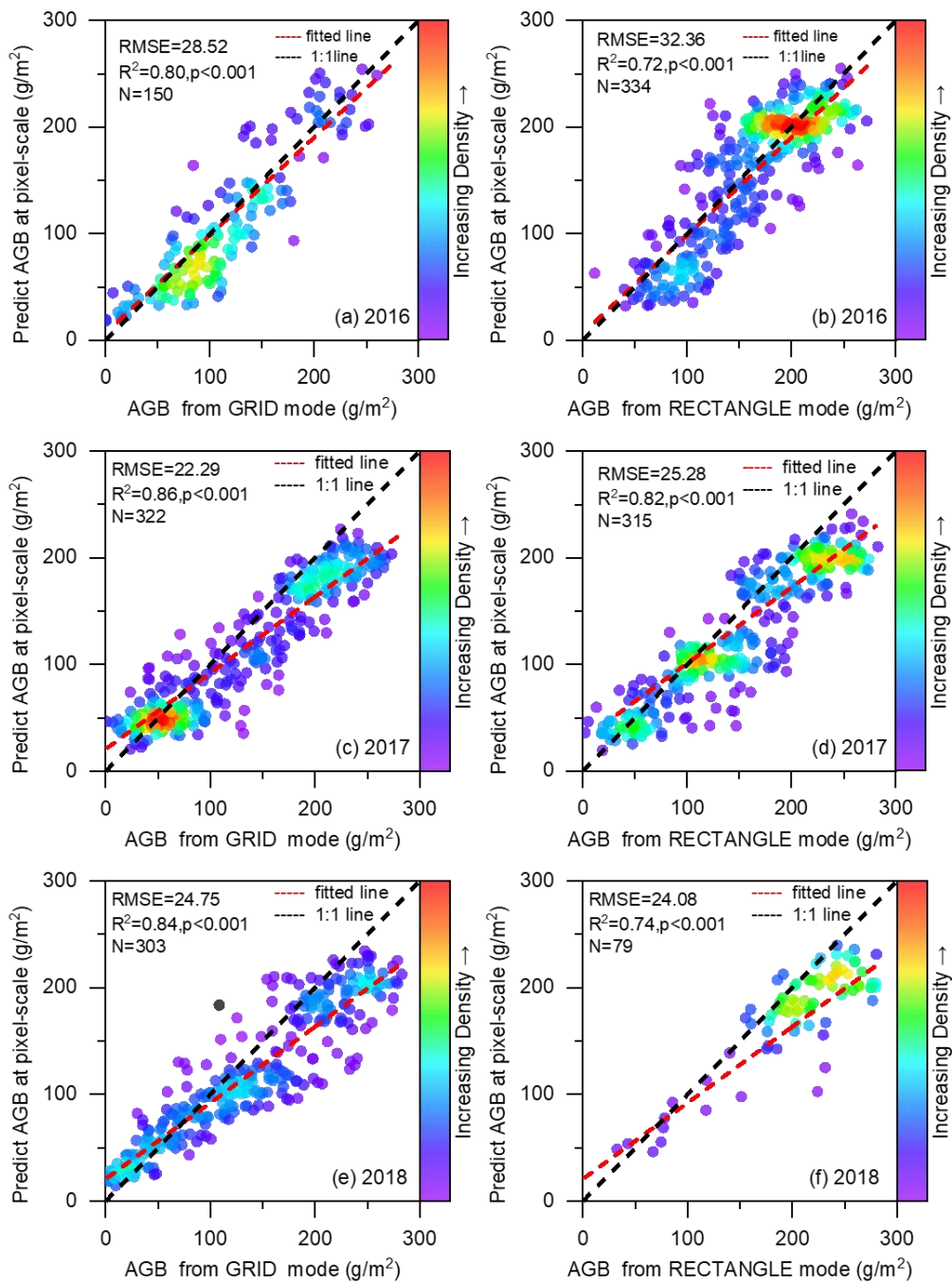
Figure 11. Comparison of validation results for the GRID (a,c,e) and RECTANGLE (b,d,f) modes in 2016-2018.

**4.2 Importance of the addition of non-vegetation samples**

Compared with traditional sampling (Yang et al., 2017), UAV sampling has the advantage of larger spatial coverage area (0.5 m × 0.5 m vs. 35 m × 26 m). Thus, the UAV photo could capture non-vegetation background information, such as roads, water, soil, gravel, and riverbed (Figure A5). Adding non-vegetation samples could improve the accuracy of AGB estimation at the photo scale, especially for areas with low vegetation cover. It was also suitable for the pixel-scale AGB estimation model.

**4.3 Comparison of the estimated AGB with previous studies**

We compared our results with previous studies at the quadrat, pixel, and regional scales. At the quadrat scale, consistent with our previous study, we further confirmed that the UAV photos could be used to estimate grassland AGB (Zhang et al., 2022a; Zhang et al., 2018). Similar to the 2-meter-high UAV photo, the 20-meter-high UAV photo could be used to estimate the grassland AGB at the quadrat scale ($R^2 = 0.73$, RMSE = 44.23 g·m$^{-2}$, Figure 6a). Compared with the 2-meter-high UAV photo (0.8 m × 1 m), the 20-meter-high UAV photo (26 m × 35 m) is more suitable for matching the MODIS pixel due to its larger spatial coverage area. In addition, the direct use of the 20-meter-high photo eliminates the need for spatial scale conversions when upscaling the AGB estimation from the quadrat scale to the photo scale.

At the pixel scale, compared with other studies, this paper achieved the spatial scale matching of independent and dependent variables during the modeling. In previous studies (Yang et al., 2009; Yang et al., 2017; Meng et al., 2020), they constructed the models from the measured AGB values at the quadrat scale and the spectral indices of the satellites without considering the spatial scale difference. It partly explained why the $R^2$ of the AGB linear model constructed by Yang et al. (2009) was only 0.4. Our results confirmed that the $R^2$ of the linear model could be increased from 0.29 to 0.78 after filling the spatial gap between measured AGB and MODIS NDVI (Figure 7). In addition, thanks to the rapid sampling of UAV technology, a total of 2,602 UAV samples matching the MODIS pixel scale were collected during 2015-2019. It allowed us to perform multi-year validation to assess the robustness of the model over time, which has rarely been performed in previous studies. Our results showed similar validation results for 2017-2019, despite different sample amounts and spatial distributions (Figure 1, Table 1). But in 2015-2016, $R^2$ was relatively low, at 0.63 and 0.77, respectively (Table 3, Figure 6). The reason was that during 2015-2016, some photos with unnatural white balance were obtained due to improper settings, which reduced the estimation accuracy (Figure A6). The validation results showed that the MODIS pixel-scale AGB estimation model had good robustness in different regions and times whenever the photo quality was acceptable.

At the regional scale, consistent with previous results, we found an overall increase in AGB over the QTP from 2000 to 2019, albeit with fluctuations (Zeng et al., 2019; Gao et al., 2020). The annual average AGB of grassland was 103.6 g·m$^{-2}$, which was closest to Zhang et al.(2022b) and within the range of the previous estimates (59.63-120.73 g·m$^{-2}$) (Table 5). The mean

411     AGB varied among different grassland types, with 151.85 g·m$^{-2}$ for the meadow and 60.85 g·m$^{-2}$ for the steppe. Our

412     estimation results were similar to those of Zeng et al.(2019), but the overall average AGB was higher than their estimate of

413     77.12 g·m$^{-2}$. The spatial distribution of AGB was consistent with previous studies, showing a west-to-east increasing trend

414     (Zhang et al., 2022b; Xia et al., 2018). Specifically, the average AGB of OA1, IIAB1, IB1, and IIC2 eco-geographical

415     regions in the east was significantly higher than that of IID2, IID3, IC2, IID1, and ID1 regions in the west (Figure 8). In

416     general, the average AGB estimates for each eco-geographical region in this paper were similar to those reported by Zhang

417     et al. (2022b). Among them, our average AGB estimates for ID1, IID1, IID3, and IID2 regions were slightly lower, but our

418     values were closer to the measured values of these regions (Figure 8c). The reason may be that they calculated the potential

419     AGB, while we calculated the actual AGB, so our estimate was relatively low. In terms of spatial and temporal trends, the

420     data results showed that the eco-geographical regions in the northern part of the QTP demonstrated an increasing trend (IID3,

421     ID1, IID2, and IIC2), while the IC2, IIC1, and IB1 regions exhibited significant or non-significant decrease, which was

422     consistent with the results of others (Gao et al., 2020; Liu et al., 2017).

423

424     **Table 5. Comparison of AGB estimation results of different studies on the QTP**

| Mean AGB (g·m$^{-2}$) | Steppe (g·m$^{-2}$) | Meadow (g·m$^{-2}$) | Study period | Approach | Input parameter | References |
|---|---|---|---|---|---|---|
| 68.8 | 50.1 | 90.8 | 2001-2004 | Linear regression | EVI | (Yang et al., 2009) |
| __ | 22.4 | 42.37 | 2000-2012 | Linear regression | NDVI | (Liu et al., 2017) |
| 120.73 | __ | __ | 1980-2014 | Exponential regression | NDVI | (Jiao et al., 2017) |
| 78.4 | __ | __ | 1982-2010 | RF | NDVI, climate | (Xia et al., 2018) |
| 77.12 | 76.43 | 154.72 | 2000-2014 | RF | NDVI, EVI, climate, terrain | (Zeng et al., 2019) |
| 59.63 | 42.75 | 77.56 | 2000-2017 | RF | NDVI, climate | (Gao et al., 2020) |
| 102.4 | __ | __ | 2000-2020 | RF | climate, soil, and terrain | (Zhang et al., 2022b) |
| 70.00 | __ | __ | 1960-2002 | Century | climate and soil data | (Zhang et al., 2007) |
| 119.78 | __ | __ | 2002-2004 | Orchidee | climate, soil and LAI data | (Tan et al., 2010) |
| 103.6 | 60.85 | 151.85 | 2000-2019 | RF | MODIS | this study |

425

426

427     The difference between our estimated grassland AGB and previous studies might be due to differences in data sources and

428     modeling methods. Firstly, the sample amount and spatial distribution of ground samples were different. The number of

429     ground samples is the most important variable affecting the accuracy of the grassland AGB estimation model (Morais et al.,

430     2021). Unlike previous studies, we collected ground validation data by combining the traditional sampling method and

431     UAVs. The newly proposed method could overcome the shortcomings of traditional samplings (time-consuming and labor-

432     intensive). It no longer takes years to obtain spatially representative, large-scale ground validation data (Yang et al., 2017).

With UAV sampling, ground observations matching the satellite pixel scale can be obtained in only 15-20 minutes, which is difficult to achieve in traditional surveys. Our new sampling method not only accelerates the sampling speed and increases the sample amount, but also improves the spatial match between ground samples and satellite pixels. As a result, our ground validation data is better than previous studies in terms of quantity and spatial scale matching with the satellite data. Secondly, the input parameters of AGB estimation models were different. Some scholars used only a single vegetation index (NDVI or EVI), while others combined the vegetation index with meteorological, soil, and terrain indices to construct the AGB estimation models (Table 5). In this study, NDVI, kNDVI, EVI, DEM, and MAP were used as the final predictor variables to construct the AGB estimation model at the MODIS pixel scale (Table 2). Thirdly, modeling methods might also affect the estimation results. As shown in Table 5, the overall AGB averages of the QTP estimated based on different methods (such as linear or nonlinear regression, machine learning, and ecological process model methods) varied considerably. Yang et al. (2017) found that the model performance of the artificial neural network (ANN) was much better than the linear regression model when using the same dataset to estimate grassland AGB in the Three-River Headwaters Region of China. Jia et al. (2016) reported that the model forms could bring 13% uncertainty to the AGB estimation. Wang et al. (2017) compared the RF with the bagging, mboost, and support vector regression (SVR) algorithms, and found that the RF yielded the best performance in grassland AGB estimation.

## 4.4 Limitations and further work

We acknowledge that there are some shortcomings in this study. 1) The predicted values of the quadrat-scale model were underestimated when the measured biomass values were greater than 250 g·m$^{-2}$ (Figure 6). One of the reasons may be that the number of samples larger than 250 g·m$^{-2}$ at the quadrat scale is relatively small, accounting for only 5.18% of the total samples. Another possible reason is that the height of the grassland could not be detected by a single UAV photo. Therefore, it could lead to an underestimation of AGB for grassland species with the same FVC but greater heights. Previous studies have shown that adding vegetation height information can improve the estimation accuracy of grassland AGB (Zhang et al., 2022a; Lussem et al., 2019; Viljanen et al., 2018). In future work, an affordable DJI Zensil L1 Lidar UAV will be introduced to detect the height of the grassland. 2) At the MODIS pixel scale, limited by the estimation accuracy of AGB from UAV photos, there was also some underestimation in the high biomass area. Although the MODIS indices closest to the sampling date were chosen for the construction/validation of the AGB estimation model, there was still a time gap between the measured samples and the MODIS indices, which might lead to estimation uncertainties. In addition, the NDVI saturation problem was not considered in this study, which might affect the AGB estimation accuracy in QTP (Tucker, 1979a; Gao et al., 2000; Mutanga and Skidmore, 2004; Tucker, 1979b). In the next step, we will continue to collect samples with high biomass and try to correct the NDVI saturation problem for optimizing the simulation accuracy of the dataset. 3) During 2015-2016, we set the automatic white balance mode for UAV shooting due to inexperience. As a result, some photos with unnatural white balance were obtained, reducing the accuracy of AGB estimation at the photo scale (Figure A6). 4) We

collected grassland AGB only during the peak growing season, and the applicability of the proposed method to other growing seasons needs further study. 5) During the modeling process, due to the poor positioning accuracy, only the center points of the flight path were used to find the corresponding MODIS pixels. Moreover, although the UAV photos in GRID or RECTANGLE mode could cover most areas of a MODIS pixel, full pixel coverage was still not achieved. Therefore, we will gradually upscale to MODIS pixels by combining UAVs with Sentinel-2 or Landsat images.

## 5 Data availability

The dataset is available from the National Tibetan Plateau/Third Pole Environment Data Center (https://doi.org/10.11888/Terre.tpdc.272587). The dataset contains 20 years of AGB spatial data of the QTP with a resolution of 250 m and is stored in TIFF format. The name of the file is "AGB_yyyy.tif", where yyyy represents the year. For example, AGB_2000.tif represents this TIFF file describing the alpine grassland AGB condition of QTP in 2000. The data can be readily imported into standard geographical information system software (e.g., ArcGIS) or accessed programmatically (e.g., MATLAB, Python).

## 6 Conclusion

This study developed a new AGB dataset for alpine grasslands on the QTP based on traditional ground sampling, UAV photography, and MODIS imagery. The uniqueness of this dataset is the use of UAVs as a spatial scale-matching bridge between traditional samples and MODIS pixels. The study confirmed that the UAV photos could be used for AGB estimation at the quadrat/MODIS pixel scale, with $R^2$ of 0.73/0.83 and RMSE of 44.23/34.13 $g \cdot m^{-2}$, respectively. At the MODIS pixel scale, the correlations between AGB estimated by UAV and MODIS vegetation indices were higher than that between field harvested AGB and MODIS vegetation indices. Moreover, the spatial scale matching of the dependent and the independent variables was achieved during the modeling. In addition, we performed a multi-year validation of the MODIS pixel-scale AGB estimation model to confirm the robustness of the model and the accuracy of this dataset. The availability of the new dataset is helpful in many applications. First, this dataset provides reliable regional data for estimating grassland productivity, carbon storage, ecological carrying capacity, and ecological service functions (such as feed for grazing livestock) of the QTP. Second, the dataset can be used to understand the mechanisms of environmental processes, such as hydrological cycle processes, soil erosion and degradation, and carbon cycle processes in the QTP. In addition, this dataset can be used as input or validation parameters for various ecological models to understand the response mechanism of the QTP to global climate change.

## 7 Author contributions

HZ contributed to the study conceptualization, methodology, funding acquisition, and the original draft of the manuscript. ZT, BW, and HK contributed to resources and formal analysis. YQ and YS contributed to data collection and manuscript review. BM, ML, and JC contributed to the methodology and reviewed the manuscript. YL and JZ participated in reviewing and editing the manuscript. SN contributed to the data collection and review of the manuscript. SY contributed to the study conceptualization, funding acquisition, and manuscript review. All authors have read and approved the manuscript.
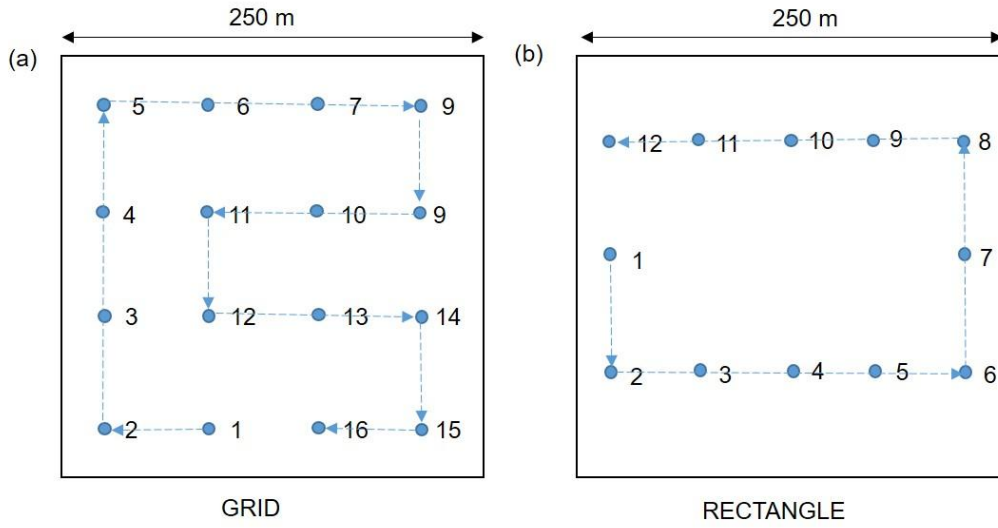
## 8 Competing interests

The authors declare that they have no conflict of interest.

## 9 Acknowledgements

## 10 Financial support

508 **Appendix**



509
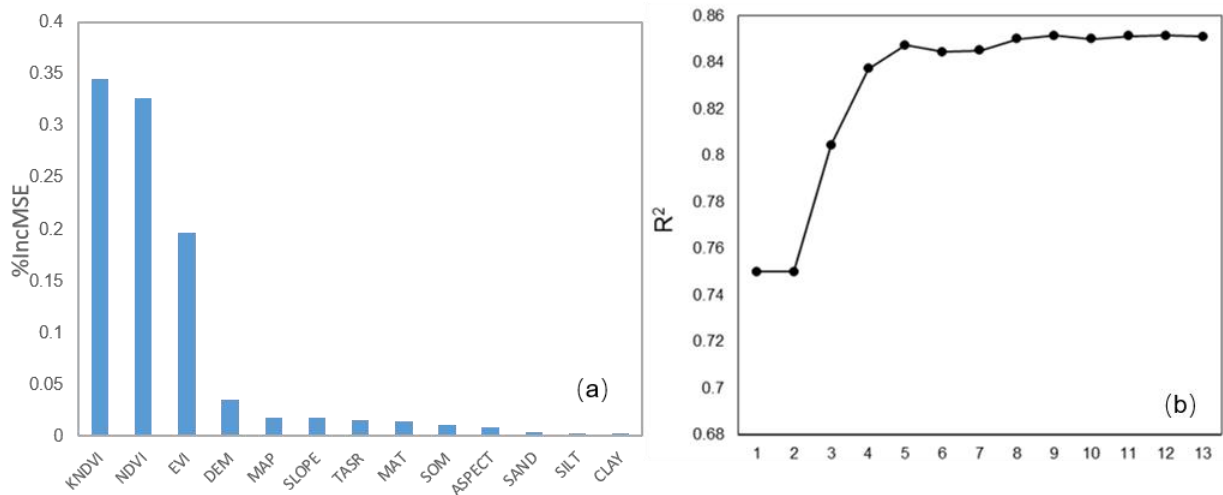510 **Figure A1. Waypoints for GRID (a) and RECTANGLE (b) flight modes.**
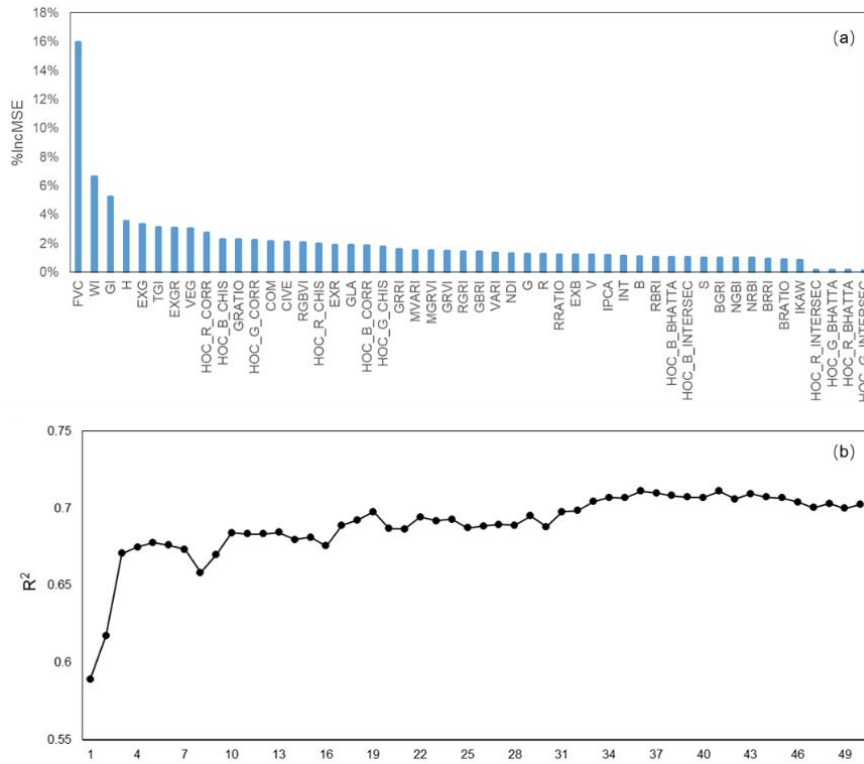


511
512 **Figure A2. The importance values for each independent variable (a) and the R² results of the different number of input variables**
513 **at the quadrat scale.**

27

514



515
516
517  **Figure A3. The importance values for each independent variable (a) and the $R^2$ results of the different number of input variables**
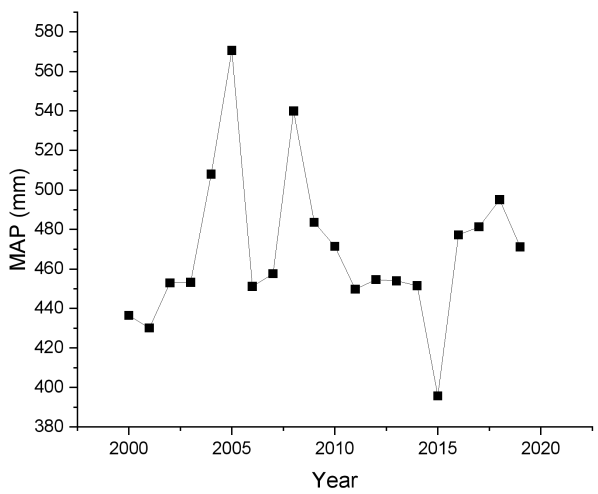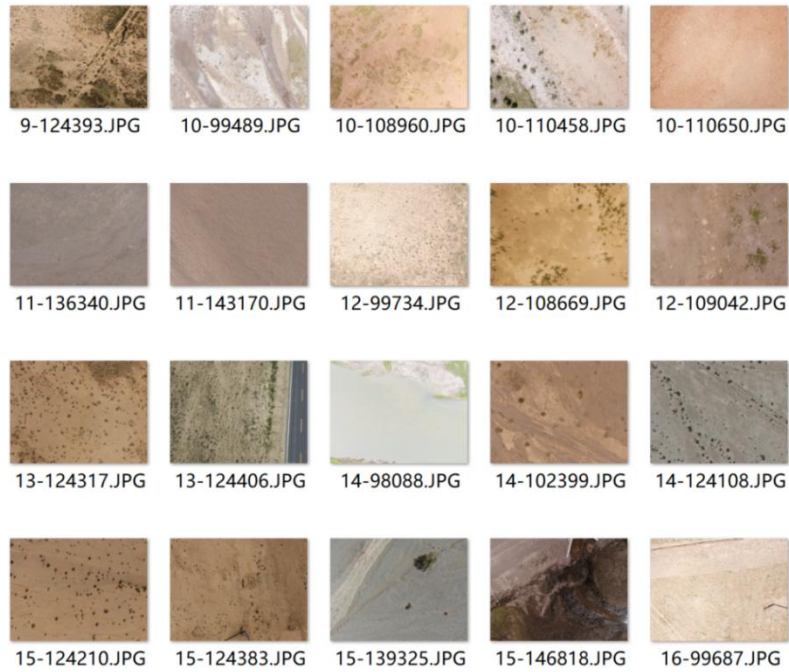518  **at the MODIS pixel scale.**



519
520  **Figure A4. Mean annual precipitation (MAP) on the QTP from 2000-2019.**
521

9-124393.JPG 10-99489.JPG 10-108960.JPG 10-110458.JPG 10-110650.JPG

11-136340.JPG 11-143170.JPG 12-99734.JPG 12-108669.JPG 12-109042.JPG

13-124317.JPG 13-124406.JPG 14-98088.JPG 14-102399.JPG 14-124108.JPG

15-124210.JPG 15-124383.JPG 15-139325.JPG 15-146818.JPG 16-99687.JPG

522

523 **Figure A5. Examples of 20-meter-high UAV photos with different non-vegetation background information.**



DJI_0064.JPG DJI_0065.JPG DJI_0066.JPG DJI_0067.JPG

DJI_0068.JPG DJI_0069.JPG DJI_0070.JPG DJI_0071.JPG

DJI_0072.JPG DJI_0073.JPG DJI_0074.JPG DJI_0075.JPG

DJI_0076.JPG DJI_0077.JPG DJI_0078.JPG DJI_0079.JPG
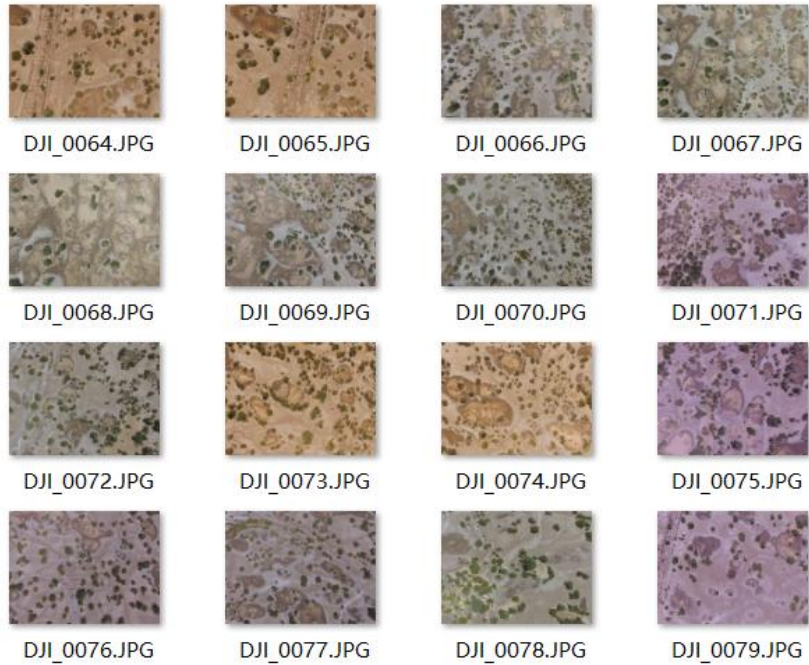
524

525 **Figure A6. An example of a set of GIRD photos with unnatural white balance in 2015.**

526

527 **Table A1. Combined grassland types**

| New grassland type | Original grassland type |
| --- | --- |
| Meadow | Alpine meadow, Lowland meadow, Montane meadow， |
| Steppe | Temperate steppe, Alpine steppe, Alpine meadow steppe |
| Desert | Temperate steppe desert, Alpine desert |

528

529

530

531 **Table A2. Features of DJI Phantom 3 Pro**

| | Features | Description |
| --- | --- | --- |
| | Sensor | 1/23-inch; Effective-pixel: 12-megapixel |
| | Field of view | FOV 94° 20 mm |
| | Aperture | f/2.8 |
| | Shooting speed | Electronic shutter: 8-1/8000 s |
| | Photo size | 4000×3000 |
| | Flight time | ~25 min |
| DJI Phantom 3 Pro | Image format | JPEG |
| | Hovering accuracy | ±0.5 m vertically; ±1.5 m horizontally |
| | Weight | 1280 g |

532

533

534 **Table A3. Details of the independent variables for quadrat-scale AGB estimation**

| Acronym | Index name | Formula | Reference |
|---------|-----------|---------|-----------|
| GRVI | Green Red Vegetation Index | (G-R)/(G+R) | (Tucker, 1979a) |
| EXG | Excess Green Vegetation Index | 2G-R-B | (Woebbecke et al., 1995) |
| GLA | Green leaf area | (2G-R-B)/(2G+R+B) | (Louhaichi et al.) |
| MGRVI | Modified Green Blue Vegetation Index | (G2-R2)/(G2+R2) | (Bendig et al., 2015) |
| RGBVI | Red Green Blue Vegetation Index | (G2-B*R)/(G2+B*R) | (Bendig et al., 2015) |
| EXB | Excess Blue Vegetation Index | (1.4*B-G)/(G+R+B) | (Maimaitijiang et al., 2019) |
| NDI | Normalized difference index | (R-G)/(R+G) | (Woebbecke et al., 1993) |
| EXR | Excess Red Vegetation Index | 1.4*R-B | (Meyer and Neto, 2008) |
| EXGR | Excess Green minus Excess Red index | ExG−ExR | (Meyer and Neto, 2008) |
| RRATIO | Red Ratio | R/(R+B+G) | (Woebbecke et al., 1995) |
| BRATIO | Blue Ratio | B/(R+B+G) | (Woebbecke et al., 1995) |
| GRATIO | Green Ratio | G/(R+B+G) | (Woebbecke et al., 1995) |
| VARI | Visible Atmospherically Resistance Index | (G -R)/(G + R - B) | (Gitelson et al., 2002) |
| NRBI | Normalized Red Blue Index | (R-B)/(R+B) | (Michez et al., 2016) |
| NGBI | Normalized Green Blue Index | (G-B)/(G+B) | (Michez et al., 2016) |
| VEG | Vegetative index | G/(RaB(1-a)),where a = 0.667 | (Hague et al., 2006) |
| WI | Woebbecke Index | (G−B)/(R−G) | (Woebbecke et al., 1995) |
| CIVE | Color Index of Vegetation | 0.441R − 0.881G+0.385B+18.78745 | (Kataoka et al., 2003) |
| COM | Combination Vegetative index | 0.25ExG+0.3ExGR+0.33CIVE +0.12VEG | (Guijarro et al., 2011) |
| TGI | Triangular Greenness Index | G-0.39R-0.61B | (Hunt et al., 2014; Michez et al., 2018) |
| RGBVI | Red Green Blue Vegetation Index | (G2-B*R)/(G2+B*R) | (Bendig et al., 2015) |
| GRRI | Green Red Ratio Index | G/R | (Maimaitijiang et al., 2019) |
| GBRI | Green Blue Ratio Index | G/B | (Maimaitijiang et al., 2019) |
| RBRI | Red Blue Ratio Index | R/B | (Maimaitijiang et al., 2019) |
| BRRI | Blue Red Ratio Index | B/R | (Jibo et al., 2018) |
| BGRI | Blue Green Ratio Index | B/G | (Jibo et al., 2018) |
| RGRI | Red Green Ratio Index | R/G | (Jibo et al., 2018) |
| INT | Color Intensity Index | (R+B+G)/3 | (Ahmad and Reid, 1996) |
| MVARI | Modified VARI | (G-B)/(G+R-B) | (Cen et al., 2019) |
| IPCA | Principal Component Analysis Index | 0.994×\|R−B\|+ 0.961×\|G−B\|+ 0.914×\|G−R\| | (Saberioon et al., 2014) |

535

536

537

**Table A3. Details of the independent variables for quadrat-scale AGB estimation (continued)**

| Acronym | Index name | Formula | Reference |
|---|---|---|---|
| R | An average value of R channel of the quadrat-scale UAV photo | | |
| G | An average value of G channel of the quadrat-scale UAV photo | | |
| B | An average value of B channel of the quadrat-scale UAV photo | | |
| H | An average value of H channel of the quadrat-scale image in HSV color space | | |
| S | An average value of S channel of the quadrat-scale image in HSV color space | | |
| V | An average value of V channel of the quadrat-scale image in HSV color space | | |
| FVC | Fractional Vegetion Cover | | |
| EGI | Extra Geen Index | EGI = 2G-R-B | |
| GI | Green Index | GI = 9×(H×3.14159/180) +3×S+V | (Zhang et al., 2022a) |
| HOC_i_CORR | The histogram correlation coefficient between the i band and the black reference histogram, where the i represents the three bands of RGB | $corr = \dfrac{\sum_I (H_1(I) - \bar{H}_1)(H_2(I) - \bar{H}_2)}{\sqrt{\sum_I (H_1(I) - \bar{H}_1)^2 \sum_I (H_2(I) - \bar{H}_2)^2}}$ | |
| HOC_i_INTERSEC | The histogram intersection coefficient between the i band and the black reference histogram, where the i represents the three bands of RGB | $intersec = \sum_I \min(H_1(I), H_2(I))$ | |
| HOC_i_BHATTA | The histogram Bhattacharyya distance coefficient between the i band and the black reference histogram, where the i represents the three bands of RGB | $bhatta = \sqrt{1 - \dfrac{1}{\sqrt{\bar{H}_1 \bar{H}_2 N^2}} \sum_I \sqrt{H_1(I) \cdot H_2(I)}}$ | |
| HOC_i_CHIS | The histogram correlation coefficient between the i band and the black reference histogram, where the i represents the three bands of RGB. | $chis = \sum_I \dfrac{(H_1(I) - H_2(I))^2}{H_1(I)}$ | |

Table A4. Regression analysis for AGB estimation models at quadrat and pixel scales

| Model name | Coefficient | Value | Standard Error | t-Value | p-value |
|---|---|---|---|---|---|
| 2019_Quadrat-scale | Slope | 0.67 | 0.016 | 42.58 | 9.05e-194 |
| | Intercept | 20.10 | 1.49 | 13.59 | 5.96e-37 |
| 2019_Pixel_scale | Slope | 0.84 | 0.03 | 31.59 | 2.75e-73 |
| | Intercept | 23.20 | 4.04 | 5.74 | 4.24e-8 |
| 2018_Pixel_scale | Slope | 0.73 | 0.02 | 45.81 | 8.28e-157 |
| | Intercept | 20.43 | 2.74 | 7.46 | 6.01e-13 |
| 2017_Pixel_scale | Slope | 0.75 | 0.01 | 59.13 | 1.98e-260 |
| | Intercept | 13.89 | 2.04 | 6.82 | 2.19e-11 |
| 2016_Pixel_scale | Slope | 0.94 | 0.02 | 40.45 | 4.69e-157 |
| | Intercept | 2.48 | 3.75 | 0.66 | 0.03 |
| 2015_Pixel_scale | Slope | 0.82 | 0.04 | 18.88 | 2.59e-47 |
| | Intercept | 9.50 | 5.25 | 1.81 | 0.04 |

Table A5. List of abbreviations of eco-geographical regions of the QTP

| Abbreviation | Full name |
|---|---|
| IB1 | Golog-Nagqu high-cold shrub-meadow zone |
| IC1 | Southern Qinghai high-cold meadow steppe zone |
| IC2 | Qiangtang high-cold steppe zone |
| ID1 | Kunlun high-cold desert zone |
| IIAB1 | Western Sichuan-eastern Tibet montane coniferous forest zone |
| IIC1 | Southern Tibet montane shrub-steppe zone |
| IIC2 | Eastern Qinghai-Qilian montane steppe zone |
| IID1 | Nagri montane desert-steppe and desert zone |
| IID2 | Qaidam montane desert zone |
| IID3 | Northern slopes of Kunlun montane desert zone |
| OA1 | Southern slopes of Himalaya montane evergreen broad-leaved forest zone |

**References**

Ahmad, I. S. and Reid, J. F.: Evaluation of Colour Representations for Maize Images, Journal of Agricultural Engineering Research, 63, 185-195, doi:10.1006/jaer.1996.0020 1996.4

Bendig, J., Yu, K., Aasen, H., Bolten, A., Bennertz, S., Broscheit, J., Gnyp, M. L., and Bareth, G.: Combining UAV-based plant height from crop surface models, visible, and near infrared vegetation indices for biomass monitoring in barley, International Journal of Applied Earth Observation & Geoinformation, 39, 79-87, doi:10.1016/j.jag.2015.02.012, 2015.4

Bian, L. and Walsh, S. J.: Scale dependencies of vegetation and topography in a mountainous environment of Montana, The Professional Geographer, 45, 1-11, doi:10.1111/j.0033-0124.1993.00001.x, 1993.4

Breiman, L.: Random forests, Machine learning, 45, 5-32, doi:10.1023/A:1010933404324, 2001.4

Camps-Valls, G., Campos-Taberner, M., Moreno-Martinez, A., Walther, S., Duveiller, G., Cescatti, A., Mahecha, M. D., Munoz-Mari, J., Garcia-Haro, F. J., Guanter, L., Jung, M., Gamon, J. A., Reichstein, M., and Running, S. W.: A unified vegetation index for quantifying the terrestrial biosphere, Sci Adv, 7, eabc7447, doi:10.1126/sciadv.abc7447, 2021.4

Cannavacciuolo, M., Bellido, A., Cluzeau, D., Gascuel, C., and Trehen, P.: A geostatistical approach to the study of earthworm distribution in grassland, Applied Soil Ecology, 9, 345-349, doi:10.1016/S0929-1393(98)00087-0, 1998.4

Cen, H. Y., Wan, L., Zhu, J. P., Li, Y. J., Li, X. R., Zhu, Y. M., Weng, H. Y., Wu, W. K., Yin, W. X., Xu, C., Bao, Y. D., Feng, L., Shou, J. Y., and He, Y.: Dynamic monitoring of biomass of rice under different nitrogen treatments using a lightweight UAV with dual image-frame snapshot cameras, Plant Methods, 15, doi:10.1186/s13007-019-0418-8, 2019.4

Chen, J., Yi, S., Qin, Y., and Wang, X.: Improving estimates of fractional vegetation cover based on UAV in alpine grassland on the Qinghai–Tibetan Plateau, International Journal of Remote Sensing, 37, 1922-1936, doi:10.1080/01431161.2016.1165884, 2016.4

Cheng, X., An, S., Chen, J., Li, B., Liu, Y., and Liu, S.: Spatial relationships among species, above-ground biomass, N, and P in degraded grasslands in Ordos Plateau, northwestern China, Journal of Arid Environments, 68, 652-667, doi:10.1016/j.jaridenv.2006.07.006, 2007.4

Crow, W. T., Berg, A. A., Cosh, M. H., Loew, A., Mohanty, B. P., Panciera, R., de Rosnay, P., Ryu, D., and Walker, J. P.: Upscaling sparse ground‐based soil moisture observations for the validation of coarse‐resolution satellite soil moisture products, Reviews of Geophysics, 50, doi:10.1029/2011rg000372, 2012.4

Dancy, K., Webster, R., and Abel, N.: Estimating and mapping grass cover and biomass from low-level photographic sampling, International Journal of Remote Sensing, 7, 1679-1704, doi:10.1080/01431168608948961, 1986.4

Ding, M. J., Zhang, Y. L., Sun, X. M., Liu, L. S., Wang, Z. F., and Bai, W. Q.: Spatiotemporal variation in alpine grassland phenology in the Qinghai-Tibetan Plateau from 1999 to 2009, Chinese Science Bulletin, 58, 396-405, doi:10.1007/s11434-012-5407-5, 2013.4

Dusseux, P., Hubert-Moy, L., Corpetti, T., and Vertes, F.: Evaluation of SPOT imagery for the estimation of grassland biomass, International Journal of Applied Earth Observation and Geoinformation, 38, 72-77, doi:10.1016/j.jag.2014.12.003, 2015.4

Fensholt, R., Rasmussen, K., Nielsen, T. T., and Mbow, C.: Evaluation of earth observation based long term vegetation trends—Intercomparing NDVI time series trend analysis consistency of Sahel from AVHRR GIMMS, Terra MODIS and SPOT VGT data, Remote sensing of environment, 113, 1886-1898, 2009.4

Gao, X., Huete, A. R., Ni, W., and Miura, T.: Optical–biophysical relationships of vegetation spectra without background contamination, Remote sensing of environment, 74, 609-620, 2000.4

Gao, X. X., Dong, S. K., Li, S., Xu, Y. D., Liu, S. L., Zhao, H. D., Yeomans, J., Li, Y., Shen, H., Wu, S. N., and Zhi, Y. L.: Using the random forest model and validated MODIS with the field spectrometer measurement promote the accuracy of estimating aboveground biomass and coverage of alpine grasslands on the Qinghai-Tibetan Plateau, Ecological Indicators, 112, 106114, doi:10.1016/j.ecolind.2020.106114, 2020.4

Ghosh, S. M. and Behera, M. D.: Aboveground biomass estimation using multi-sensor data synergy and machine learning algorithms in a dense tropical forest, Applied Geography, 96, 29-40, doi:10.1016/j.apgeog.2018.05.011, 2018.4

Gitelson, A. A., Kaufman, Y. J., Stark, R., and Rundquist, D.: Novel algorithms for remote estimation of vegetation fraction, Remote Sensing of Environment, 80, 76-87, doi:10.1016/s0034-4257(01)00289-9 2002.4

Guijarro, M., Pajares, G., Riomoros, I., Herrera, P. J., Burgos-Artizzu, X. P., and Ribeiro, A.: Automatic segmentation of relevant textures in agricultural images, Computers & Electronics in Agriculture, 75, 75-83, doi:10.1016/j.compag.2010.09.013, 2011.4

Hague, T., Tillett, N. D., and Wheeler, H.: Automated Crop and Weed Monitoring in Widely Spaced Cereals, Precision Agriculture, 7, 21-32, doi:10.1007/s11119-005-6787-1, 2006.4

He, L., Li, A. N., Yin, G. F., Nan, X., and Bian, J. H.: Retrieval of Grassland Aboveground Biomass through Inversion of the PROSAIL Model with MODIS Imagery, Remote Sensing, 11, 1597, doi:10.3390/rs11131597, 2019.4

Hoaglin, D. C., Mosteller, F., and Tukey, J. W.: Understanding robust and exploratory data anlysis, Wiley series in probability and mathematical statistics, 1983.4

Holben, B. N.: Characteristics of maximum-value composite images from temporal AVHRR data, International journal of remote sensing, 7, 1417-1434, 1986.4

Hunt, E. R., Daughtry, C. S. T., Mirsky, S. B., and Hively, W. D.: Remote Sensing With Simulated Unmanned Aircraft Imagery for Precision Agriculture Applications, IEEE Journal of Selected Topics in Applied Earth Observations & Remote Sensing, 7, 4566-4571, doi:doi:10.1109/jstars.2014.2317876, 2014.4

Jia, W., Liu, M., Yang, Y., He, H., Zhu, X., Yang, F., Yin, C., and Xiang, W.: Estimation and uncertainty analyses of grassland biomass in Northern China: Comparison of multiple remote sensing data sources and modeling approaches, Ecological indicators, 60, 1031-1040, doi:10.1016/j.ecolind.2015.09.001, 2016.4

Jiang, W., Yuan, L., Wang, W., Cao, R., Zhang, Y., and Shen, W.: Spatio-temporal analysis of vegetation variation in the Yellow River Basin, Ecological Indicators, 51, 117-126, 2015.4

Jiao, C., Yu, G., He, N., Ma, A., and Hu, Z.: The spatial pattern of grassland aboveground biomass and its environmental controls in the Eurasian steppe, doi:10.11821/dlxb201605007, 2017.4

Jibo, Y., Haikuan, F., Xiuliang, J., Huanhuan, Y., Zhenhai, L., Chengquan, Z., Guijun, Y., and Qingjiu, T.: A Comparison of Crop Parameters Estimation Using Images from UAV-Mounted Snapshot Hyperspectral Sensor and High-Definition Digital Camera, Remote Sensing, 10, 1138-, doi:10.3390/rs10071138, 2018.4

Kataoka, T., Kaneko, T., Okamoto, H., and Hata, S.: Crop growth estimation system using machine vision, Advanced Intelligent Mechatronics, 2003. AIM 2003. Proceedings. 2003 IEEE/ASME International Conference on, Crop growth estimation system using machine vision,

Kohavi, R.: A study of cross-validation and bootstrap for accuracy estimation and model selection, Ijcai, 1137-1145, doi:10.1109/jstars.2014.2317876,

Li, M., Wu, J., Feng, Y., Niu, B., He, Y., and Zhang, X.: Climate variability rather than livestock grazing dominates changes in alpine grassland productivity across Tibet, Frontiers in Ecology and Evolution, 9, doi:10.3389/fevo.2021.631024, 2021.4

Li, X., Liu, S., Li, H., Ma, Y., Wang, J., Zhang, Y., Xu, Z., Xu, T., Song, L., and Yang, X.: Intercomparison of six upscaling evapotranspiration methods: From site to the satellite pixel, Journal of Geophysical Research: Atmospheres, 123, 6777-6803, doi:10.1029/2018jd028422, 2018.4

Liu, S., Cheng, F., Dong, S., Zhao, H., Hou, X., and Wu, X.: Spatiotemporal dynamics of grassland aboveground biomass on the Qinghai-Tibet Plateau based on validated MODIS NDVI, Scientific reports, 7, 1-10, doi:10.1038/s41598-017-04038-4, 2017.4

Louhaichi, M., Borman, M. M., and Johnson, D.: Spatially Located Platform and Aerial Photography for Documentation of Grazing Impacts on Wheat, Geocarto International, doi:10.1080/10106040108542184,

Lussem, U., Bolten, A., Menne, J., Gnyp, M. L., Schellberg, J., and Bareth, G.: Estimating biomass in temperate grassland with high resolution canopy surface models from UAV-based RGB images and vegetation indices, Journal of Applied Remote Sensing, 13, 034525, doi:10.1117/1.Jrs.13.034525, 2019.4

Maimaitijiang, M., Sagan, V., Sidike, P., Maimaitiyiming, M., Hartling, S., Peterson, K. T., Maw, M. J. W., Shakoor, N., Mockler, T., and Fritschi, F. B.: Vegetation Index Weighted Canopy Volume Model (CVM VI) for soybean biomass estimation from Unmanned Aerial System-based RGB imagery, ISPRS Journal of Photogrammetry and Remote Sensing, 151, 27-41, doi:10.1016/j.isprsjprs.2019.03.003, 2019.4

Meng, B., Yi, S., Liang, T., Yin, J., and Sun, Y.: Modeling alpine grassland above ground biomass based on remote sensing data and machine learning algorithm: A case study in the east of Tibetan Plateau, China, IEEE Journal of Selected Topics in Applied Earth Observations and Remote Sensing, PP, 1-1, doi:10.1109/Jstars.2020.2999348, 2020.4

Meyer, G. E. and Neto, J. C.: Verification of color vegetation indices for automated crop imaging applications, Computers and Electronics in Agriculture, 63, 282-293, doi:10.1016/j.compag.2008.03.009, 2008.4

Michez, A., Piégay, H., Lisein, J., Claessens, H., and Lejeune, P.: Classification of riparian forest species and health condition using multi-temporal and hyperspatial imagery from unmanned aerial system, Environmental Monitoring & Assessment, 188, 1-19, doi:10.1007/s10661-015-4996-2, 2016.4

Michez, A., Bauwens, S., Brostaux, Y., Hiel, M. P., Garré, S., Lejeune, P., and Dumont, B.: How Far Can Consumer-Grade UAV RGB Imagery Describe Crop Production? A 3D and Multitemporal Modeling Approach Applied to Zea mays, Remote Sensing, 10, doi:10.3390/rs10111798, 2018.4

Morais, T. G., Teixeira, R. F., Figueiredo, M., and Domingos, T.: The use of machine learning methods to estimate aboveground biomass of grasslands: A review, Ecological Indicators, 130, 108081, doi:10.1016/j.ecolind.2021.108081, 2021.4

Mutanga, O. and Skidmore, A. K.: Narrow band vegetation indices overcome the saturation problem in biomass estimation, International journal of remote sensing, 25, 3999-4014, 2004.4

Mutanga, O., Adam, E., and Cho, M. A.: High density biomass estimation for wetland vegetation using WorldView-2 imagery and random forest regression algorithm, International Journal of Applied Earth Observation and Geoinformation, 18, 399-406, doi:10.1016/j.jag.2012.03.012, 2012.4

Ómara, F. P.: The role of grasslands in food security and climate change, Annals of botany, 110, 1263-1270, doi:10.1093/aob/mcs209, 2012.4

Ramankutty, N., Evan, A. T., Monfreda, C., and Foley, J. A.: Farming the planet: 1. Geographic distribution of global agricultural lands in the year 2000, Global biogeochemical cycles, 22, doi:10.1029/2007GB002952, 2008.4

Saberioon, M. M., Amin, M., Anuar, A. R., Gholizadeh, A., Wayayok, A., and Khairunniza-Bejo, S.: Assessment of rice leaf chlorophyll content using visible bands at different growth stages at both the leaf and canopy scale, International Journal of Applied Earth Observations & Geoinformation, 32, 35-45, doi:10.1016/j.jag.2014.03.018, 2014.4

Suttie, J. M., Reynolds, S. G., and Batello, C.: Grasslands of the World, Food & Agriculture Org.2005.

Tan, K., Ciais, P., Piao, S., Wu, X., Tang, Y., Vuichard, N., Liang, S., and Fang, J.: Application of theORCHIDEE global vegetationmodel to evaluate biomass and soil carbon stocks ofQinghai-Tibetan grasslands, 2010.4

Tucker, C. J.: Red and photographic infrared linear combinations for monitoring vegetation, Remote Sensing and Environment, 8, 127-150, doi:10.1016/0034-4257(79)90013-0, 1979a.4

Tucker, C. J.: Red and photographic infrared linear combinations for monitoring vegetation, Remote sensing of Environment, 8, 127-150, 1979b.4

Vergara, J. R. and Estévez, P. A.: A review of feature selection methods based on mutual information, Neural computing and applications, 24, 175-186, doi:10.1007/s00521-013-1368-0, 2014.4

Viljanen, N., Honkavaara, E., Näsi, R., Hakala, T., Niemeläinen, O., and Kaivosoja, J.: A novel machine learning method for estimating biomass of grass swards using a photogrammetric canopy height model, images and vegetation indices captured by a drone, Agriculture, 8, 70, doi:10.3390/agriculture8050070, 2018.4

Wang, J. and Sun, W.: Multiscale geostatistical analysis of sampled above-ground biomass and vegetation index products from HJ-1A/B, Landsat, and MODIS, Land Surface Remote Sensing II, 2014.11, 335-344, doi:10.1117/12.2069008,

Wang, J., Ge, Y., Song, Y., and Li, X.: A geostatistical approach to upscale soil moisture with unequal precision observations, IEEE Geoscience and Remote Sensing Letters, 11, 2125-2129, doi:10.1109/Lgrs.2014.2321429, 2014.4

Wang, J., Xiao, X., Bajgain, R., Starks, P., Steiner, J., Doughty, R. B., and Chang, Q.: Estimating leaf area index and aboveground biomass of grazing pastures using Sentinel-1, Sentinel-2 and Landsat images, ISPRS Journal of Photogrammetry and Remote Sensing, 154, 189-201, doi:10.1016/j.isprsjprs.2019.06.007, 2019.4

Wang, L. a., Zhou, X., Zhu, X., Dong, Z., and Guo, W.: Estimation of biomass in wheat using random forest regression algorithm and remote sensing data, The Crop Journal, 4, 212-219, doi:10.1016/j.cj.2016.01.008, 2016.4

Wang, Y., Shen, X., Jiang, M., Tong, S., and Lu, X.: Spatiotemporal change of aboveground biomass and its response to climate change in marshes of the Tibetan Plateau, International Journal of Applied Earth Observation and Geoinformation, 102, 102385, 2021.4

Wang, Y., Wu, G., Deng, L., Tang, Z., Wang, K., Sun, W., and Shangguan, Z.: Prediction of aboveground grassland biomass on the Loess Plateau, China, using a random forest algorithm, Scientific reports, 7, 1-10, doi:10.1038/s41598-017-07197-6, 2017.4

Woebbecke, D. M., Meyer, G. E., Bargen, K. V., and Mortensen, D. A.: Color Indices for Weed Identification Under Various Soil, Residue, and Lighting Conditions, Transactions of the Asae, 38, 259-269, doi:10.1109/jstars.2014.2317876 1995.4

Woebbecke, D. M., Meyer, G. E., Von Bargen, K., and Mortensen, D. A.: Plant species identification, size, and enumeration using machine vision techniques on near-binary images, Optics in Agriculture and Forestry, 208-219, 10.1117/12.144030

Xia, J., Ma, M., Liang, T., Wu, C., Yang, Y., Zhang, L., Zhang, Y., and Yuan, W.: Estimates of grassland biomass and turnover time on the Tibetan Plateau, Environmental Research Letters, 13, 014020, doi:10.1088/1748-9326/aa9997, 2018.4

Yang, S., Feng, Q., Liang, T., Liu, B., Zhang, W., and Xie, H.: Modeling grassland above-ground biomass based on artificial neural network and remote sensing in the Three-River Headwaters Region, Remote Sensing of Environment, S0034425717304741, doi:10.1016/j.rse.2017.10.011, 2017.4

Yang, Y., Fang, J., Pan, Y., and Ji, C.: Aboveground biomass in Tibetan grasslands, Journal of Arid Environments, 73, 91-95, doi:10.1016/j.jaridenv.2008.09.027, 2009.4

Yang, Y., Fang, J., Ma, W., Guo, D., and Mohammat, A.: Large‐scale pattern of biomass partitioning across China's grasslands, Global Ecology and Biogeography, 19, 268-277, doi:10.1111/j.1466-8238.2009.00502.x, 2010.4

Yi, S.: FragMAP: a tool for long-term and cooperative monitoring and analysis of small-scale habitat fragmentation using an unmanned aerial vehicle, International Journal of Remote Sensing, 38, 2686-2697, doi:10.1080/01431161.2016.1253898, 2017.4

Yu, R., Yao, Y., Wang, Q., Wan, H., Xie, Z., Tang, W., Zhang, Z., Yang, J., Shang, K., and Guo, X.: Satellite-Derived Estimation of Grassland Aboveground Biomass in the Three-River Headwaters Region of China during 1982–2018, Remote Sensing, 13, 2993, doi:10.3390/rs13152993, 2021.4

Zeng, N., Ren, X., He, H., Zhang, L., Zhao, D., Ge, R., Li, P., and Niu, Z.: Estimating grassland aboveground biomass on the Tibetan Plateau using a random forest algorithm, Ecological Indicators, 102, 479-487, doi:10.1016/j.ecolind.2019.02.023, 2019.4

Zhang, B., Zhang, L., Xie, D., Yin, X., Liu, C., and Liu, G.: Application of synthetic NDVI time series blended from Landsat and MODIS data for grassland biomass estimation, Remote Sensing, 8, 10, doi:10.3390/rs8010010, 2016.4

Zhang, H., Sun, Y., Chang, L., Qin, Y., Chen, J., Qin, Y., Du, J., Yi, S., and Wang, Y.: Estimation of grassland canopy height and aboveground biomass at the quadrat scale using unmanned aerial vehicle, Remote sensing, 10, 851, doi:10.3390/rs10060851, 2018.4

Zhang, H. F., Tang, Z. G., Wang, B. Y., Meng, B. P., Qin, Y., Sun, Y., Lv, Y. Y., Zhang, J. G., and Yi, S. H.: A non-destructive method for rapid acquisition of grassland aboveground biomass for satellite ground verification using UAV RGB images, Global Ecology and Conservation, 33, e01999, doi:10.1016/j.gecco.2022.e01999, 2022a.4

Zhang, X., LI, M., WU, J., HE, Y., and NIU, B.: Alpine Grassland Aboveground Biomass and Theoretical Livestock Carrying Capacity on the Tibetan Plateau, Journal of Resources and Ecology, 13, 129-141, 2022b.4

Zhang, Y., Bingyu, L. I., and Zheng, D.: Datasets of the boundary and area of the Tibetan Plateau, ACTA GEOGRAPHICA SINICA, 69, 164-168, 2014.4

Zhang, Y. Q., Tang, Y. H., and Jiang, J. A.: Characterizing the dynamics of soil organic carbon in grasslands on the Qinghai-Tibetan Plateau, 2007.4

Zheng, D.: Natural region system research of Tibetan Plateau, Science in China (Series D), 26, 336–334, 1996.4